

Chapter 5

Plunging Airfoil Wake Structures

In this chapter, the wake structures of a plunging airfoil are examined. Comparison is made with experimental results in the literature, and the dependence of the wake structures on the Strouhal number and the reduced frequency of the flapping motion is explored.

5.1 Introduction

As discussed in the Literature Review at Section 2.1.1, the aerodynamic force on a body in a flow may be related to the wake produced by the body. Bluff (unstreamlined) bodies such as cylinders at certain Reynolds numbers exhibit alternate vortex shedding into the wake, and produce a Karman vortex street consisting of alternating rows of clockwise (top) and anticlockwise (bottom) rotating vortices (for flow from left to right). The time-averaged velocity profile produced by such a configuration is a momentum-deficit profile, in that the mean velocity in the wake is lower than the free-stream value. Vortex pairs form ‘mushroom-like’ structures that are tilted upstream (see Figure 5.1 upper frame). The velocity profile and the upstream-tilted vortex structures are signatures that the body is producing drag.

If the rows of vortices are exchanged so that we have anticlockwise (top) and clockwise (bottom) rotating vortex rows, the configuration is known as a reverse Karman vortex street. The resulting time-averaged velocity profile is now a momentum-surfeit (jet) profile, such that the mean velocity is higher than the free-stream. The vortex pairs now form ‘mushroom’ structures that are tilted downstream (see Figure 5.1 lower frame). The momentum-surfeit velocity profile and the downstream-tilted vortex structures indicate that the body is producing a net thrust.

A pitching and plunging airfoil in 2D flow must exhibit a vortex street wake due to Kelvin’s Theorem and the fact that vortex lines cannot end in the fluid, as discussed in Chapter 2. Freymuth (1988), Koochesfahani (1989), Jones et al.

(1998) and Lai and Platzer (1999) showed through experiments that the wakes of flapping airfoils can be characterized as drag-producing or thrust-producing depending on the flapping frequency and amplitude. As the amplitude is increased, we might expect to see a transition from a drag-producing wake (where the inherent drag of the airfoil is greater than the thrust due to flapping) to a thrust producing wake (where the thrust due to flapping overcomes the inherent drag of the airfoil).

At the point where thrust due to flapping and the inherent airfoil drag exactly balance, we might expect to see a ‘neutral’ wake, where the rows of vortices are co-linear, and ‘mushroom’ vortex pairs are un-tilted. Lai and Platzer (1999) found that this is the case for a plunging airfoil at some combinations of frequency and amplitude. However at other combinations, resulting in zero net thrust, the wake structures showed much more complicated behaviour with multiple vortices shed from the airfoil for each half-cycle of airfoil motion, rather than the single vortex of the Karman vortex street model.

The vortex shedding process that leads to the wake patterns described above, and to the generation of lift and thrust, is not well understood. The objective of this study is to explore the details of wake structure formation and their dependency on plunging frequency and amplitude, for an airfoil undergoing pure sinusoidal plunging motion, including determination of whether the wake structures may be characterised solely by the Strouhal number (or equivalently the flapping parameter kh). This will encompass the role of leading and trailing edge vortex shedding, and the validity of the Kutta condition for low Reynolds number ($Re = 20,000$) high frequency flapping.

5.2 Karman and Reverse Karman Vortex Streets

The formation and stability of various vortex wake configurations are examined here. A series of discrete point vortices are released into a uniform free-stream, simulating a vortex sheet in potential flow, using the Vortex Wake Evolution (VWE) code as discussed in Chapter 4. The point of release of the vortices varies sinusoidally in a vertical plane, $x_R = 0$, $y_R = h \sin(\omega t)$. The strength of

the vortices at their time of release also varies sinusoidally at the same frequency as the motion of the release point, but with a phase shift ϕ_w such that $\Gamma = \Gamma_0 \sin(\omega t + \phi_w)$. Here positive circulation Γ indicates clockwise rotation. After being released, each individual vortex maintains a constant strength (circulation Γ).

At a phase shift $\phi_w = 0^\circ$, the vorticity is released in phase with the motion, so that the majority of the clockwise vorticity is released at the top of the motion cycle, and the anticlockwise vorticity at the bottom. We would expect this initial configuration of the vortex sheet to evolve into a ‘drag producing wake’ arrangement of discrete vortices. At $\phi_w = 180^\circ$ the situation is reversed and the sheet should evolve into a ‘thrust producing wake’ arrangement. At $\phi_w = 90^\circ$ and $\phi_w = 270^\circ$ the majority of vorticity is released at the centreline of the motion, so that a ‘neutral wake’ arrangement should result. This should also be the case when the amplitude of the motion $h = 0$, so that all vorticity is released along the centreline.

Figure 5.1 shows three different wake structures generated with motion amplitudes $h = +1.0$, $h = 0.0$, and $h = -1.0$, the latter equivalent to $h = 1.0, \phi_w = 180^\circ$. Positive (clockwise) vorticity is shown in red, negative (anticlockwise) in green. The centroid of vorticity for each half-cycle of motion is shown by the black circled dots. The wakes generated in this figure closely resemble the Karman and reverse Karman vortex streets discussed above after some distance downstream where the vortex sheet rolls up into large discrete vortices. Also shown in Figure 5.1 are the time-averaged horizontal velocity profiles in each case (horizontal scale enlarged 25 times for clarity), at a distance of 25 units downstream.

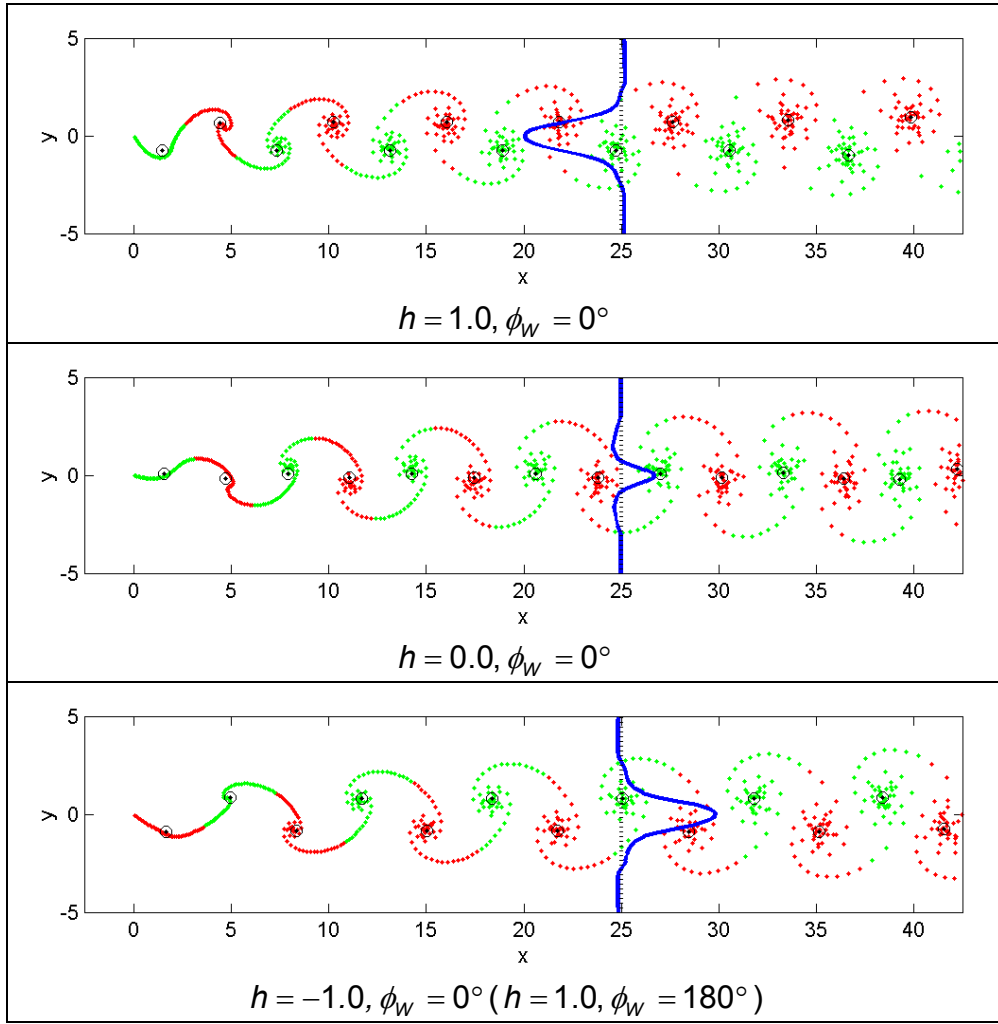


Figure 5.1. Simulated wake structures, showing drag-producing (top), approximately neutral (middle) and thrust-producing (bottom) wakes. Positive (clockwise) vorticity is shown in red, negative (anticlockwise) in green. The centroid of vorticity for each half-cycle of motion is shown by the black circled dots. Time-averaged horizontal velocity profile plotted in blue (scale enlarged 25 times).

When considering the large rolled-up vortices, pairs of vortices in the drag-producing wake form ‘mushroom’ structures that are tilted upstream. Corresponding structures in the thrust-producing wake are tilted downstream, while those in the neutral wake are essentially untilted. Note that for the neutral wake, close to the release point (near $x = 0$ in Figure 5.1), the structures appear to be tilted downstream as for a thrust-producing wake. However the positions of the vorticity centroids are closer to the centreline than would appear

by just looking at the rolled-up vortex positions. This discrepancy is reduced further downstream.

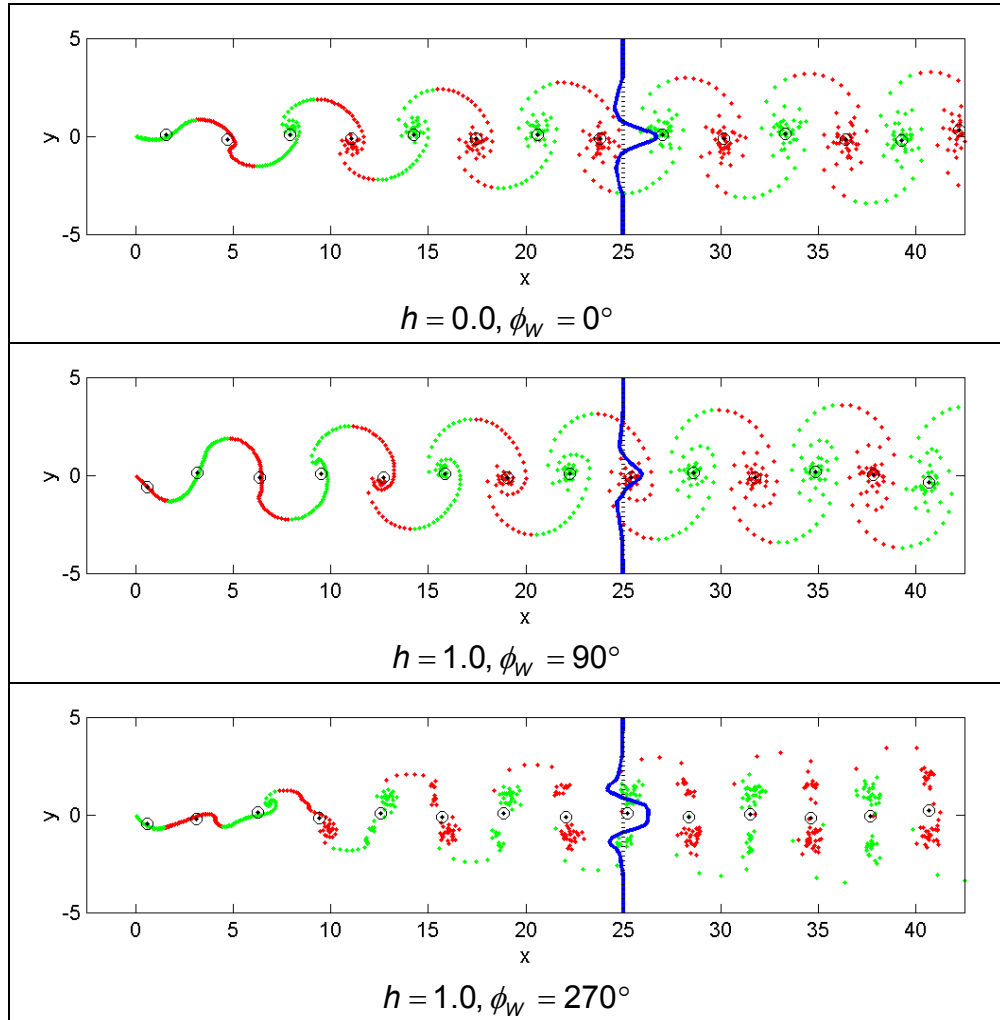


Figure 5.2. Simulated wake structures, showing three different configurations that give rise to approximately neutral wakes.

The velocity profiles clearly show a momentum deficit for the drag-producing wake, and a momentum surfeit for the thrust producing wake. For the $h = 0.0, \phi_w = 0^\circ$ case, the velocity profile shows both over and undershoots about the free-stream value, such that the total momentum surfeit is close to zero (although apparently slightly greater than zero here, in line with the slight downstream tilting of the vortex pairs), confirming that this is approximately a neutral wake.

Figure 5.2 shows three different neutral wakes, generated by varying the phase angle between the motion of the release point, and the vorticity strength. Again,

while the vorticity centroids are not perfectly aligned with the centreline, they are fairly close and discrepancies are reduced further downstream. This figure shows that a number of different vortex configurations can give rise to a neutral wake (i.e. a velocity profile that has no net momentum deficit or surfeit). All three, however, are characterised by ‘mushroom’ vortex pair structures that are untilted, that is tilted neither upstream nor downstream. It is interesting to note that the lower frame of Figure 5.2 shows two discrete vortices per half-cycle forming in the wake, a phenomenon examined further in Section 5.3.3.

Again, the velocity profiles show both over and undershoots of the free-stream value, so that the total momentum surfeit is close to zero in each case.

Figure 5.3 shows that a genuinely neutral wake can be generated by the method employed here, if the phase is selected appropriately. For the $h = 1.0, \phi_w = 80^\circ$ case, the vorticity centroids appear to be very closely aligned with the centreline, with no tilting of vortex pairs. The velocity profile in this case is almost uniformly flat, at the free-stream value.

Figure 5.4 shows the same runs as in Figure 5.1, but now with twice the amplitude of motion. The same amount of vorticity is released into the wake each half-cycle of motion as previously, but it is vertically displaced further from the centreline. Here it is clear that the resultant change in the ratio of vertical to horizontal spacing between the vortex rows still results in stable configurations. Vortex pair ‘mushroom’ structures are tilted further upstream (drag-producing) and downstream (thrust-producing) than in Figure 5.1, indicating a larger momentum deficit and surfeit respectively, which is also seen in the time-averaged velocity profiles.

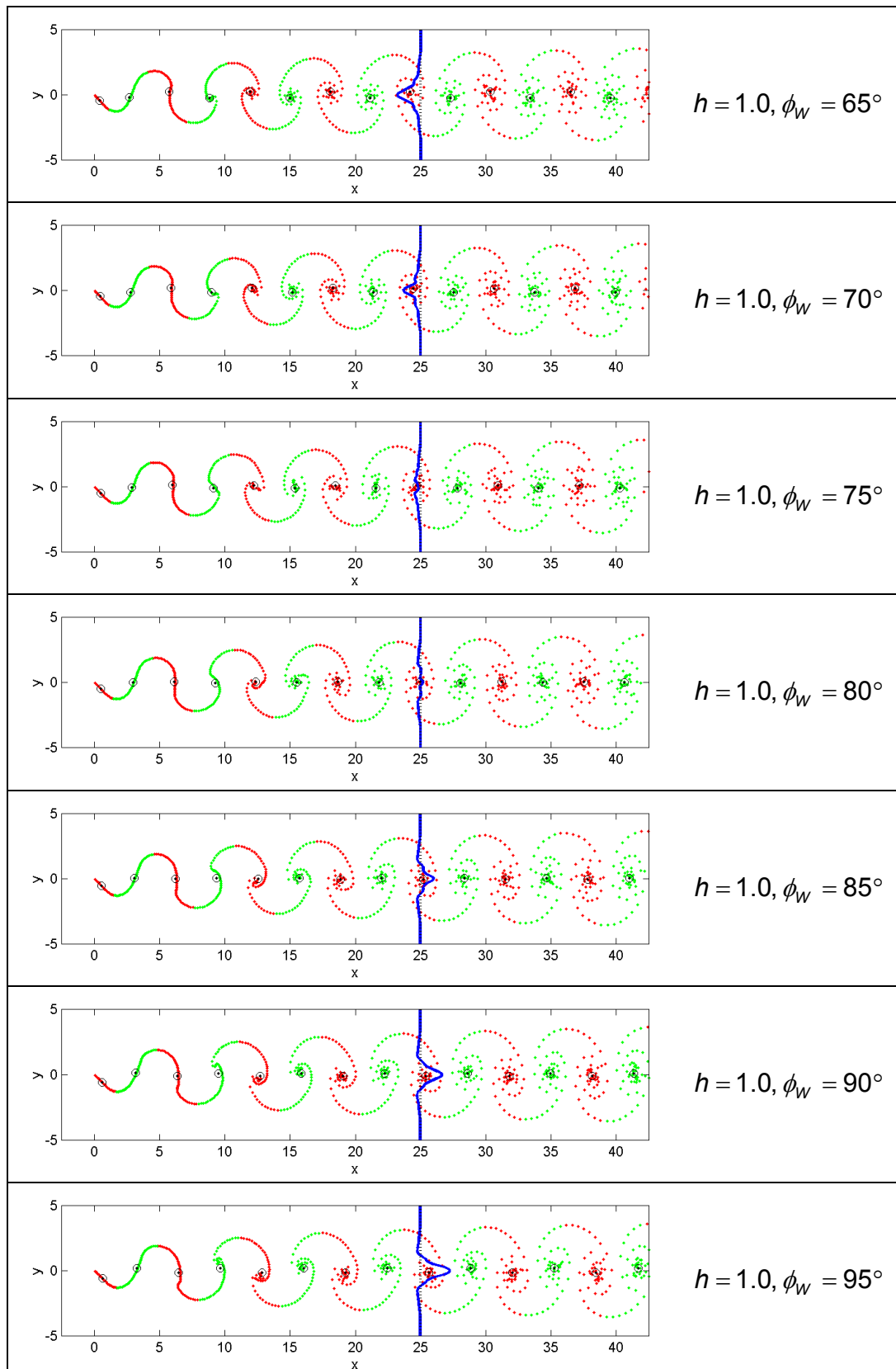


Figure 5.3. Simulated wake structures showing change from drag-producing, through neutral, to thrust-producing configurations.

We may take from the theoretical discussion and the numerical simulations of reverse Karman vortex streets, that in order to generate as much thrust as possible with a given amount of vorticity to be shed into the wake each motion cycle, the vorticity should be shed as far from the centreline of motion as possible. This conclusion is also reached by Hall and Hall (1996), who stated that for a pitching and plunging airfoil, optimum thrust is achieved when the vorticity is shed at the extremes of the trailing edge flight path.

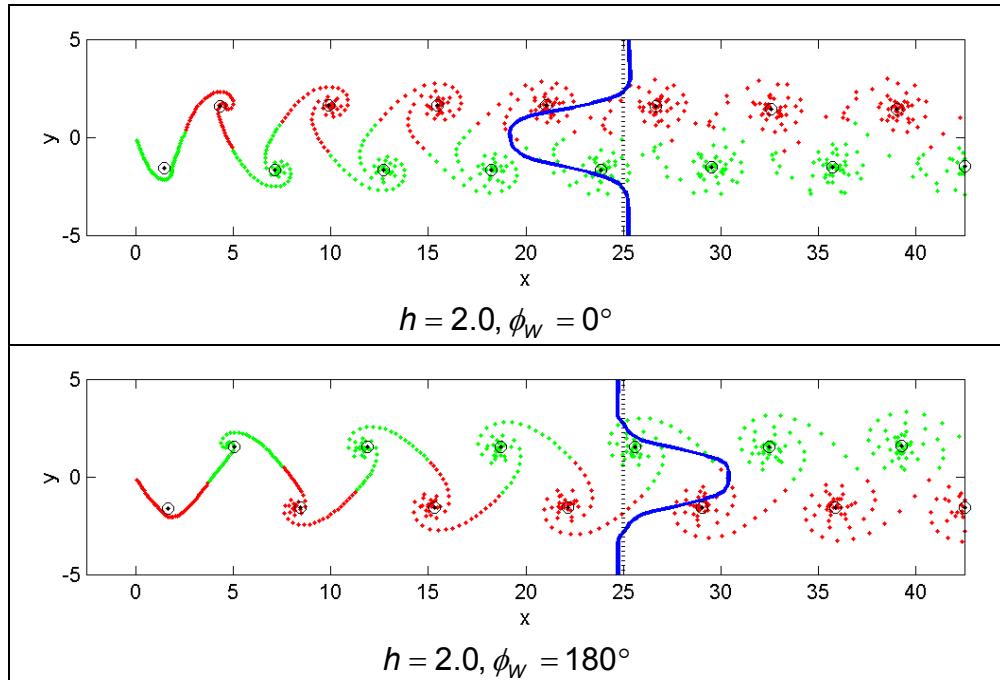


Figure 5.4. Simulated wake structures, showing larger amplitudes of motion for drag-producing and thrust-producing wakes.

5.3 Dependence of Wake Structure on Plunging Parameters

5.3.1 Predictions based on Linearised Analysis

The Garrick analysis assumes a flat wake consisting of a continuous vortex sheet that is assumed to be shed from the trailing edge of the flat plate airfoil. The strength of the vortex sheet varies in a sinusoidal manner, with some phase between the vortex strength variation and the motion of the airfoil. If the plunging motion of the airfoil is given by $y/c = h \cos(\omega t + \phi_h)$, then the strength

per unit length of the vortex sheet, at the trailing edge of the airfoil is given by $\gamma_{TE} = \gamma_0 \cos(\omega t + \phi_w)$.

The sheet is convected downstream from the airfoil at the free-stream velocity U_∞ and is fixed in shape, that is it is not allowed to roll up in response to the induced velocity field of the sheet. Thus the vortex sheet is stationary with respect to an observer travelling downstream at the free-stream velocity.

As seen in Chapter 3, for pure plunging motion the vortex sheet strength per unit length is given by:

$$\frac{\gamma_0}{U_\infty} = 4(2kh) \sqrt{\frac{F^2 + G^2}{J_1^2 + Y_1^2}} \quad (3.57)$$

The phase of the vortex strength variation is given by:

$$\phi_w - \phi_h = \tan^{-1} \left(\frac{-Y_0 - J_1}{Y_1 - J_0} \right) - k \quad (3.58)$$

The vortex strength is a function of both the frequency k , and the parameter $2kh$ (equivalent to Strouhal number), while the phase is just a function of the frequency. These quantities are plotted in Figure 5.5 and Figure 5.6.

Although the wake in the Garrick model has a fixed shape, the analysis may still be used to predict the likely wake shape when non-linear roll-up is allowed, using the VWE code of the previous section. The continuous vortex sheet is modelled as a series of discrete point vortices. In this case the vortex strength used for each individual vortex is found by multiplying the vortex sheet strength per unit length by one wavelength, divided by the number of vortices released per cycle N_{TS} , such that $\Gamma = \Gamma_0 \cos(\omega t + \phi_w)$, where $\Gamma_0 = \gamma_0 \times \frac{\pi}{k} \times \frac{1}{N_{TS}}$, so that

there is an additional $\frac{1}{k}$ variation, the result of which is shown in Figure 5.7.

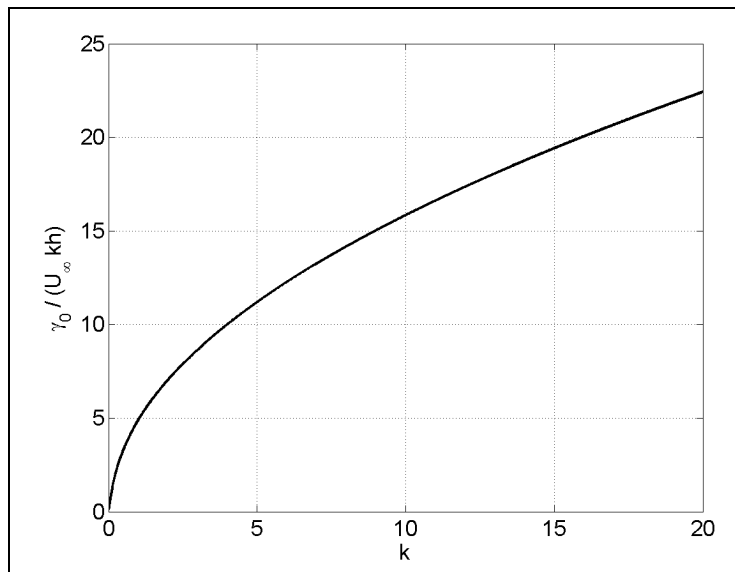


Figure 5.5. Vortex sheet strength per unit length divided by kh , as a function of plunging reduced frequency k , Garrick analysis.

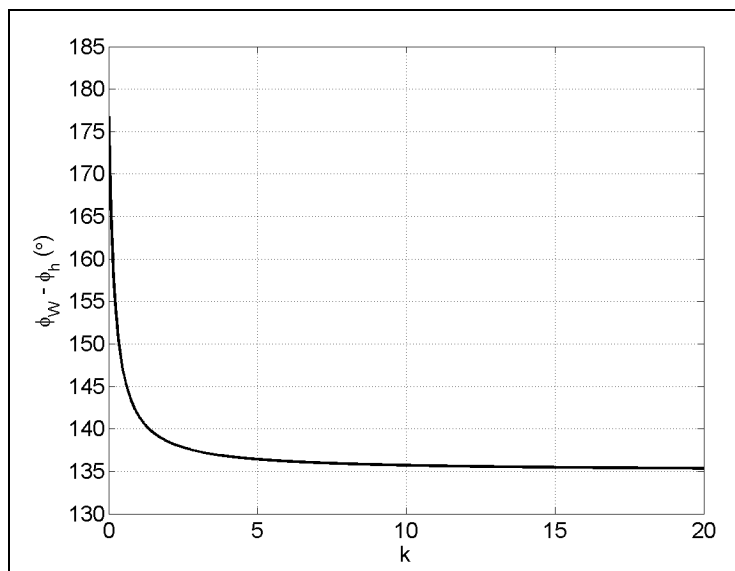


Figure 5.6. Vortex sheet strength phase angle ϕ_w compared to plunging motion phase ϕ_h , as a function of plunging reduced frequency k , Garrick analysis.

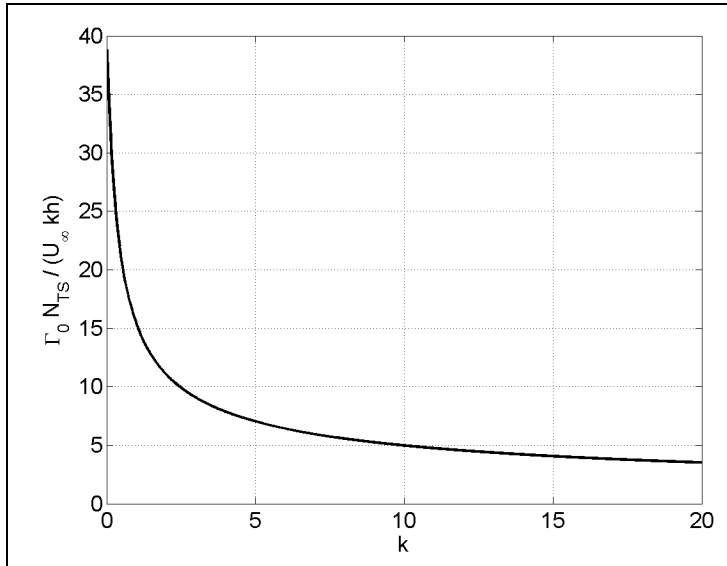


Figure 5.7. Equivalent individual vortex strength in the VWE code divided by kh , as a function of plunging reduced frequency k , Garrick analysis.

These phase and vortex strength variations are used as input to the VWE code, for a variety of different values of k and kh . The results are shown in Figure 5.8 to Figure 5.10, varying k and h while holding kh constant, for $kh = 0.1, 0.2$ and 0.3 . The phase angle plotted in Figure 5.6 varies only with frequency k , from 180° at low k to 135° at high k . This remains in the range of thrust-producing wakes, which is reflected in the wake structures seen below.

Note that the scale of each plot in Figure 5.8 to Figure 5.10 is reduced as the frequency increases. When plotted against each other in this manner, the wake configurations all look broadly geometrically similar, with more roll-up of vortices apparent as the frequency is increased. Also the vortex roll-up increases as kh is increased. The wake is no longer convected downstream at exactly the free-stream velocity as in the Garrick model, due to the additional influence of each individual wake vortex on every other vortex.

Here the vortex strength phase shift $\phi_w - \phi_h$ cannot assume arbitrary values, as was done with the VWE code in Figure 5.3. The Garrick analysis enforces the Kutta condition at the trailing edge of the airfoil, relating the sign and strength of the shed vorticity to the motion of the airfoil. A physical explanation for the vortex strength phase behaviour observed in Figure 5.6 may be gained as

follows. The strength of vorticity shed into the wake is determined by how rapidly the lift on the airfoil, and hence the angle of attack, varies with time. The angle of attack depends on the plunge velocity, thus the wake strength depends on the rate of change of the angle of attack, or the acceleration of the airfoil, which is 180° out of phase with the motion. Hence at low frequency k , $\phi_w - \phi_h = 180^\circ$. As k increases, the wake strength γ_0 increases as seen in Figure 5.5 and the wavelength decreases, and so the wake has a stronger influence on the airfoil. For example, as the airfoil moves downwards to its lowest extreme, it sheds positive (clockwise) vorticity which creates an upwash on the airfoil, raising the effective angle of attack and increasing the lift. Equally the lift is reduced as the airfoil moves upwards to its extreme upper position. The net effect is to increase the phase angle by which the lift lags the motion, which in turn increases the lag (i.e. decreases the lead) between wake vorticity and the motion. Thus we see a decrease in $\phi_w - \phi_h$ as k increases.

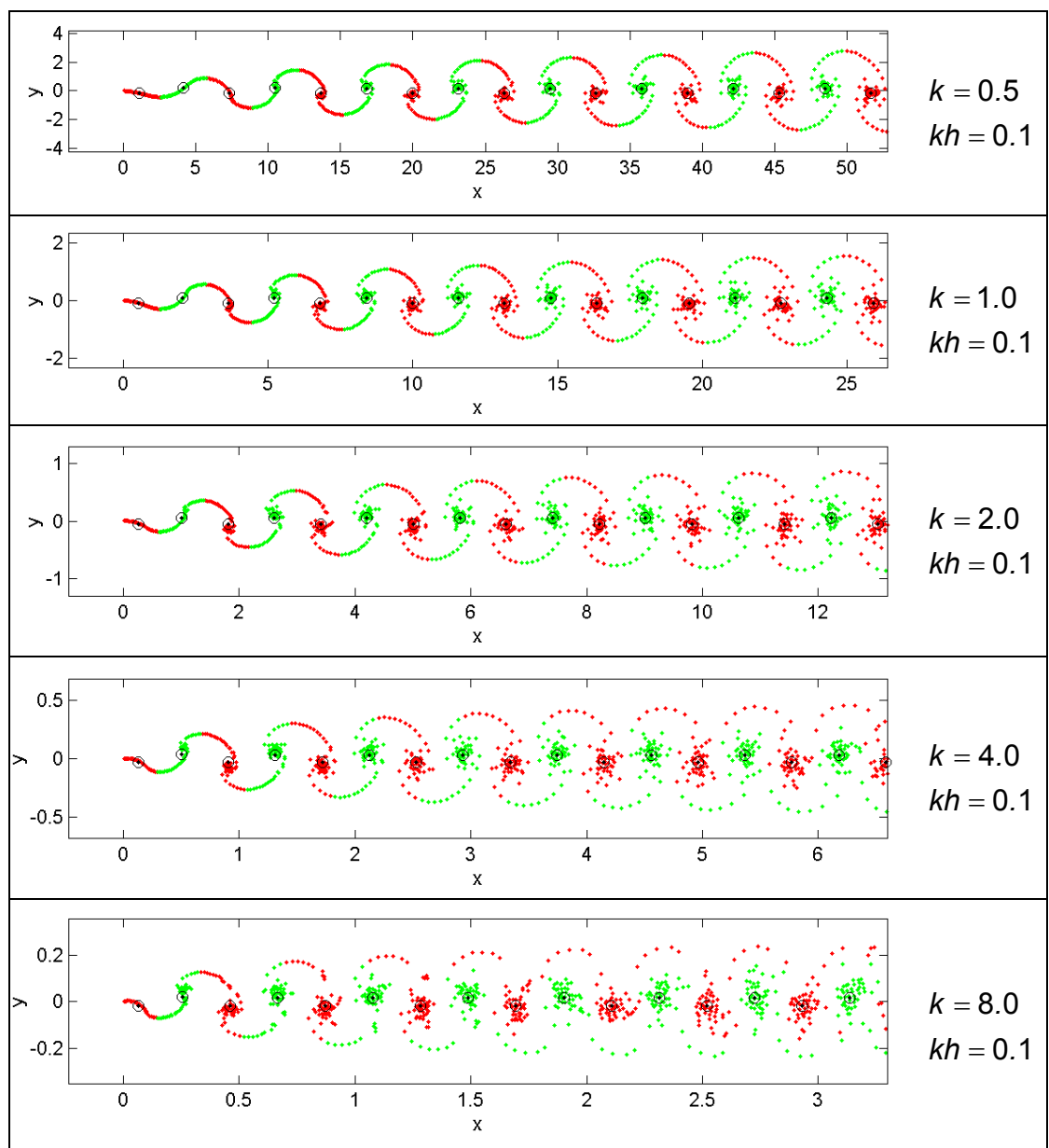


Figure 5.8. Simulated wake structures behind a flat plate airfoil,
Garrick analysis used as input to VWE code, $kh = 0.1$

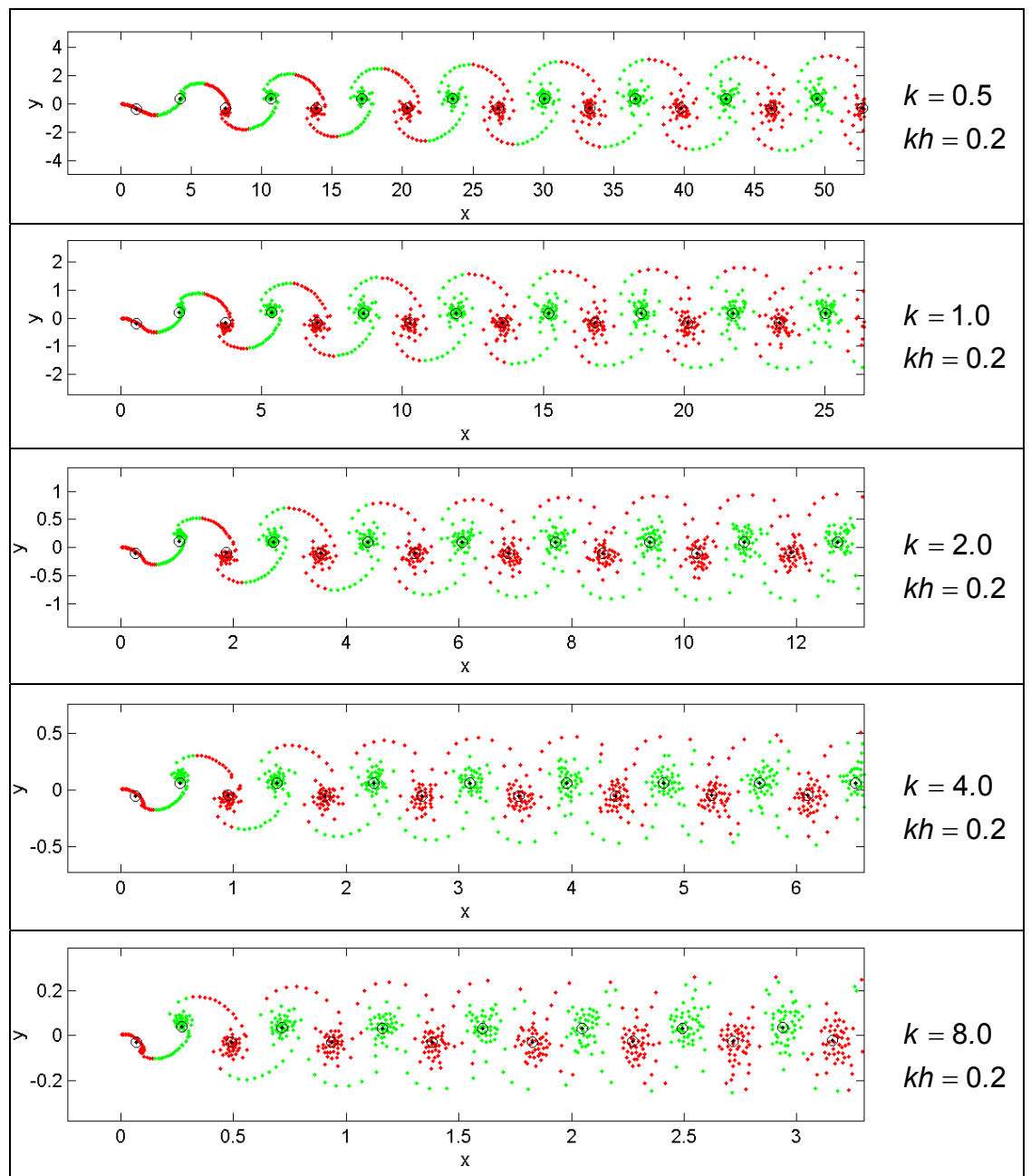


Figure 5.9. Simulated wake structures behind a flat plate airfoil,
Garrick analysis used as input to VWE code, $kh = 0.2$.

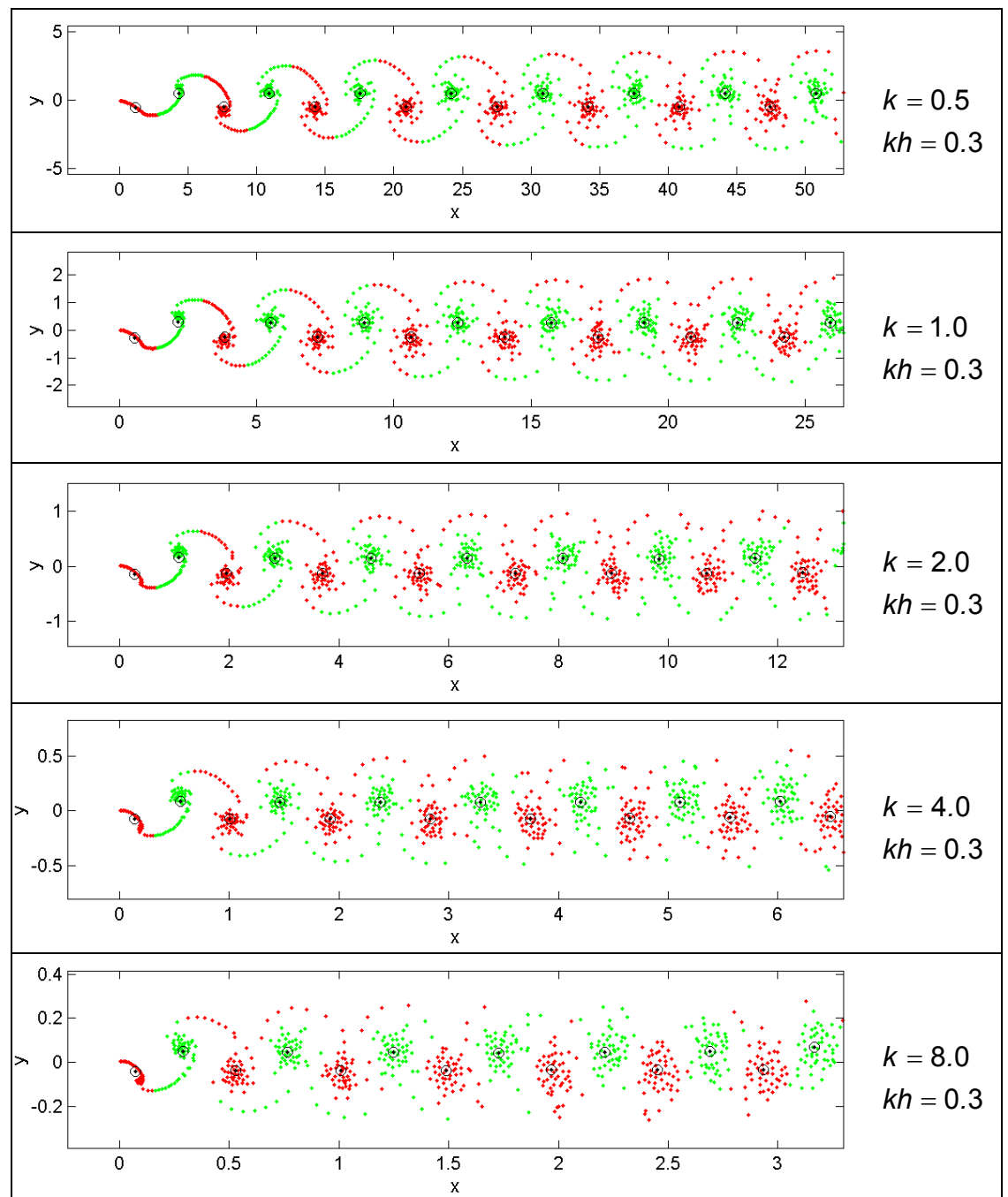


Figure 5.10. Simulated wake structures behind a flat plate airfoil,
Garrick analysis used as input to VWE code, $kh = 0.3$.

To quantify the variation in wake structure with k and kh predicted by this analysis, Figure 5.11 shows the ratio of vertical to horizontal spacing of the vorticity centroids (averaged over 5 cycles of motion) for the runs used to generate Figure 5.8 to Figure 5.10. Also shown are the spacing ratios when vortex evolution is not allowed (as in the original Garrick analysis) so that the wake remains in a sinusoidal shape, for comparison.

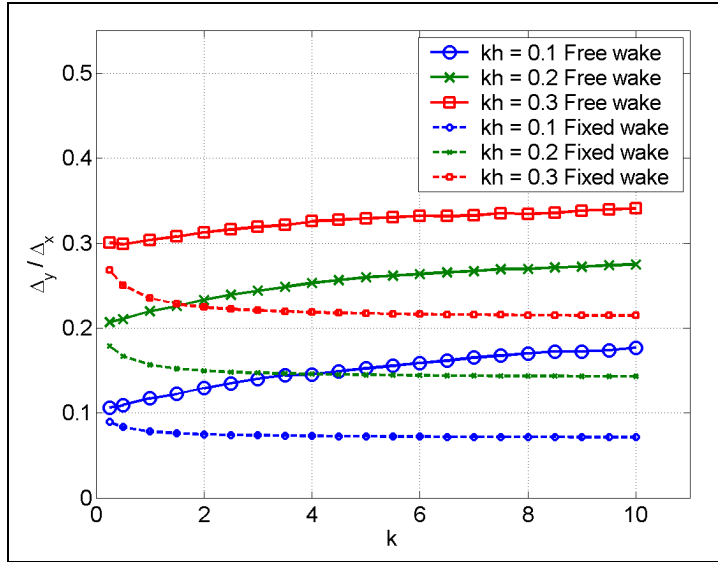


Figure 5.11. Ratio of vortex centroid spacing as a function of k and kh , for both evolving (Free) and non-evolving (Fixed) wakes, Garrick analysis used as input to VWE code.

When wake evolution is not allowed, the vortex centroid spacing asymptotes with increasing k to given value that depends on kh alone. When vortex evolution is allowed, the spacing is affected by both k and kh independently, although kh has the larger influence. This behaviour is expected since it may be shown that the vortex sheet strength is very closely approximated by:

$$\frac{\gamma_0}{U_\infty} = 4(2kh) \sqrt{\frac{F^2 + G^2}{J_1^2 + Y_1^2}} \approx \frac{1358\pi}{851} \sqrt{k(kh)} \quad (5.1.)$$

Thus the strength of each individual vortex in the VWE simulations is $\Gamma_0 / U_\infty \propto (kh)k^{-1/2}$. The velocity induced by one vortex on its neighbour is proportional to the vortex strength divided by the distance between them, and the distance is inversely proportional to frequency k , so that induced velocity

becomes $u_i / U_\infty \propto (kh)k^{1/2}$. The larger the ratio between induced and free-stream velocity, the more rapid the vortex roll-up.

The Garrick analysis, when combined with the VWE code, thus produces a wake configuration that is always thrust-producing for pure plunging motion, and predicts a wake structure determined chiefly by kh , with some effect from the frequency k .

5.3.2 Predictions of the UPM Code

The Unsteady Panel Method (UPM) code adds an additional level of realism to the prediction of wake structure, as follows. Firstly, a finite thickness airfoil is simulated rather than a flat plate, which modifies the velocity field somewhat. The velocity field that the wake experiences is also modified by the fact that as the airfoil moves and the Kutta condition is enforced, the flow around the airfoil near the trailing edge is no longer aligned with the free-stream (as in the Garrick model), but has an additional vertical component which varies sinusoidally with the motion. This results in an angle at which the flow leaves the trailing edge, producing a time-varying change in the direction in which the whole wake is convected. This angle is also accounted for in a third effect, namely that the vortices are shed from the trailing edge into the wake at an angle rather than directly downstream as in the Garrick model.

The three effects serve to modify the position at which each individual vortex is shed into the wake, and how the whole wake subsequently evolves, so it is worthwhile to examine how this additional level of realism modifies the predictions of wake structure as a function of k and kh .

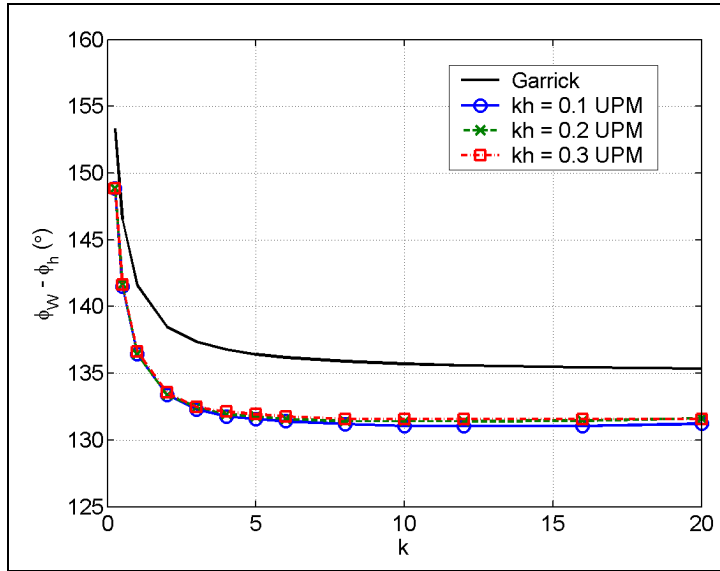


Figure 5.12. Vortex sheet strength phase angle, compared to plunging motion phase, as a function of plunging reduced frequency k , kh held constant as k varies, Garrick analysis and UPM code.

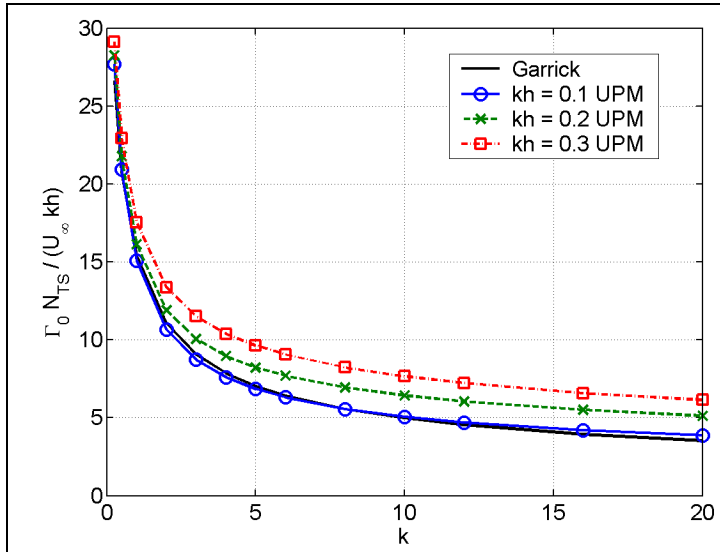


Figure 5.13. Individual wake vortex strength, as a function of plunging reduced frequency k , kh held constant as k varies, Garrick + VWE, and UPM code.

Figure 5.12 and Figure 5.13 show that the vorticity released into the wake by the UPM code, using a NACA0012 airfoil, follows very closely the behaviour predicted by the Garrick analysis for a flat plate. In the latter, the individual wake vortex strength varies linearly with kh , but in the UPM code results there is some slightly non-linear growth in strength with kh . The variation with k appears

very similar. This also applies to the phase of the vorticity compared to the phase of the motion $\phi_w - \phi_h$, in that the shape of the phase variation with k is very similar, although uniformly 4° to 5° smaller. This discrepancy is largely attributable to the difference in flow conditions at the trailing edge for the NACA0012 airfoil of the UPM calculations and the flat plate of the Garrick analysis, as evidenced by the change in phase as the thickness of the airfoil in the UPM calculations is changed from 12% to 3% and 1%, to simulate more closely a flat plate. These calculations are shown in Figure 5.14.

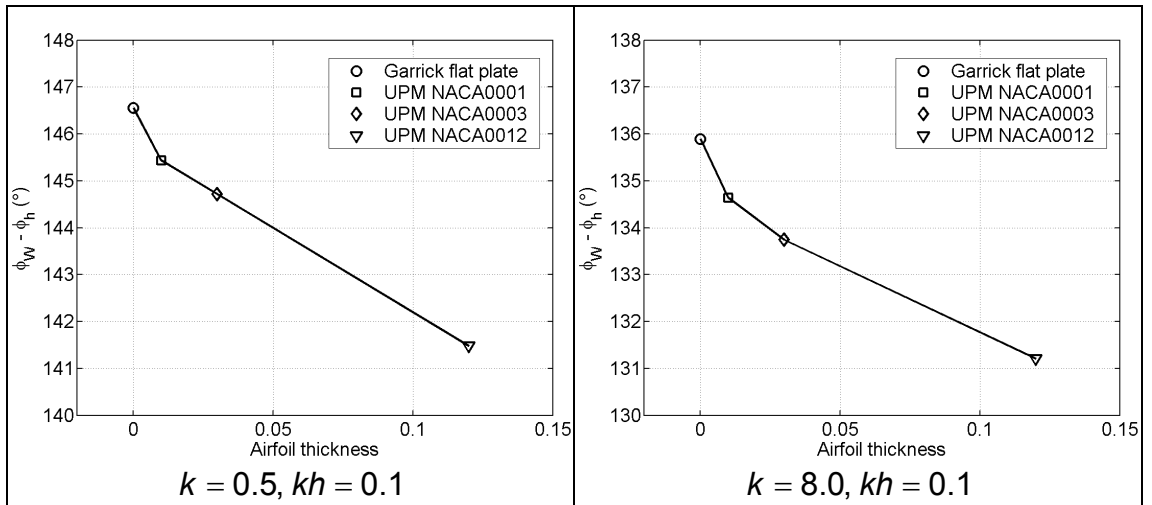


Figure 5.14. Variation of vortex strength phase angle, compared to plunging motion phase, as airfoil thickness is changed, Garrick analysis and UPM code.

Figure 5.15 to Figure 5.17 show the wake structures generated by the UPM code, for the same runs as Figure 5.8 to Figure 5.10. Again the wake structures are all broadly geometrically similar when plotted at an equivalent scale referenced to the motion of the airfoil, with increasing wake roll-up for increasing k and for increasing kh .

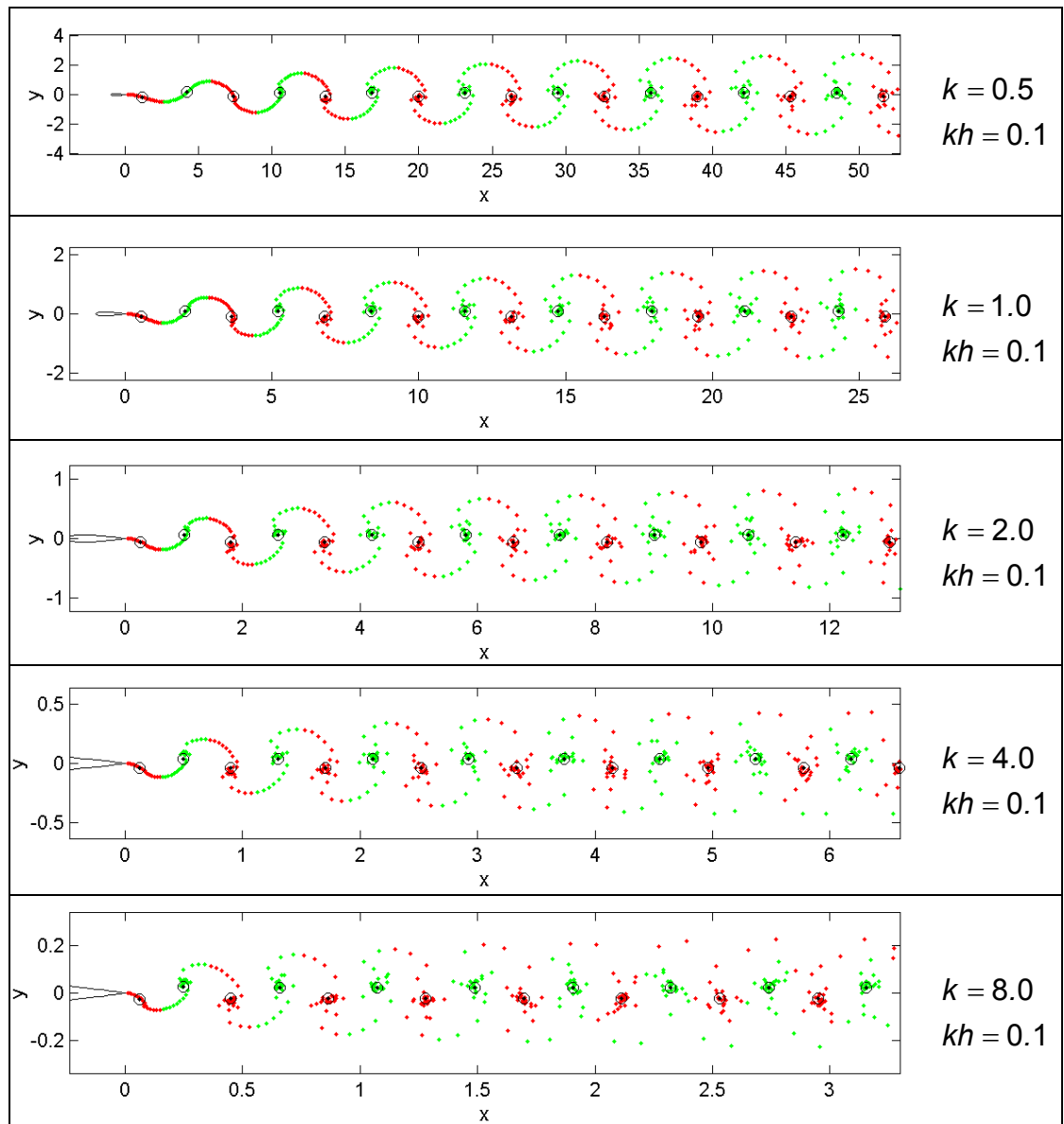


Figure 5.15. Simulated wake structures behind a NACA0012 airfoil,
UPM code, $kh = 0.1$

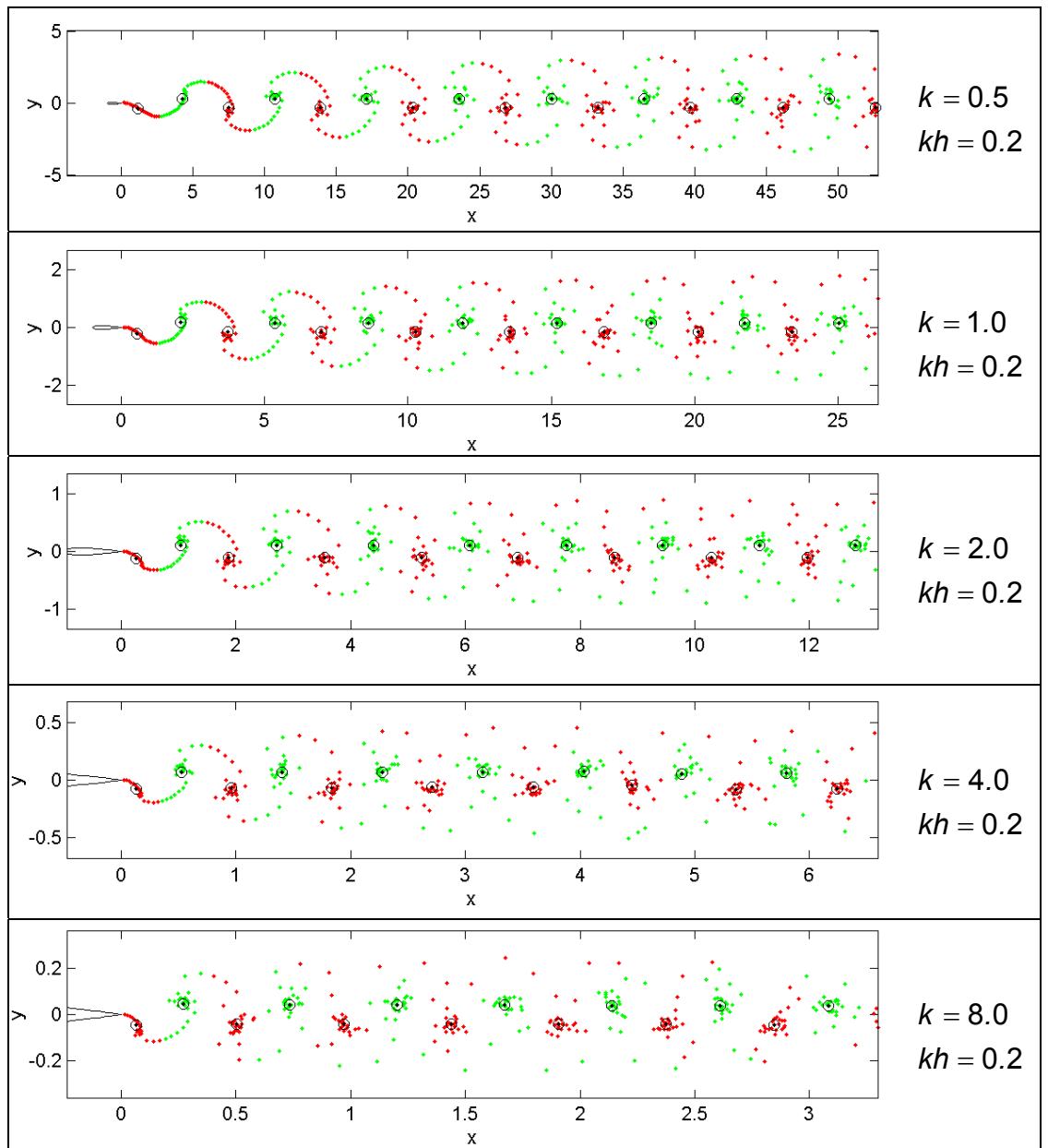


Figure 5.16. Simulated wake structures behind a NACA0012 airfoil,
UPM code, $kh = 0.2$.

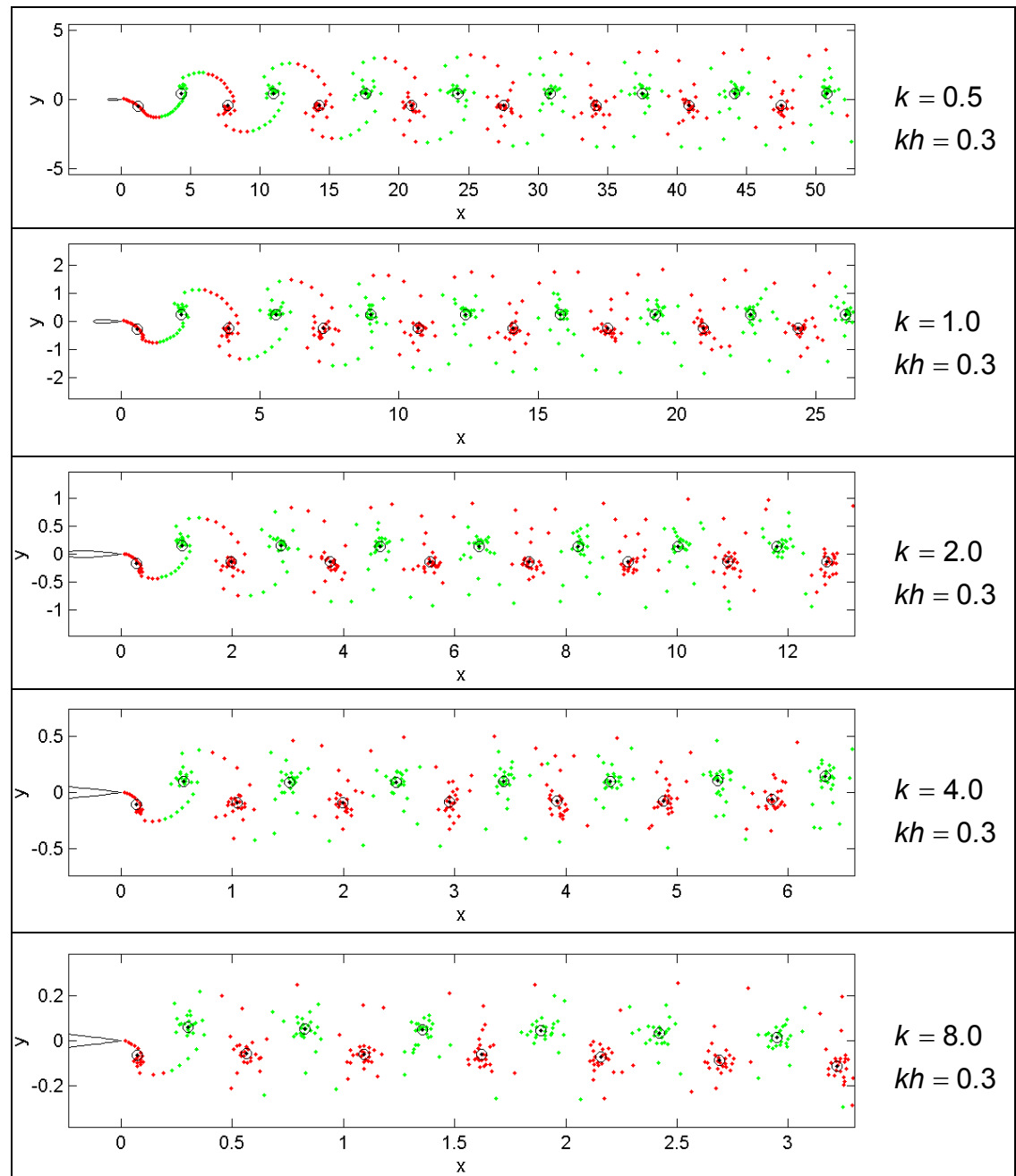


Figure 5.17. Simulated wake structures behind a NACA0012 airfoil,
UPM code, $kh = 0.3$.

It is again difficult to draw firm conclusions about variation in wake structure with k and kh from visual inspection of Figure 5.15 to Figure 5.17, so the ratio of vertical to horizontal spacing of the vorticity centroids Δ_y / Δ_x is used as a quantitative measure of the downstream tilt of the vortex pairs. This is plotted in Figure 5.18, along with the Garrick + VWE results from Figure 5.11.

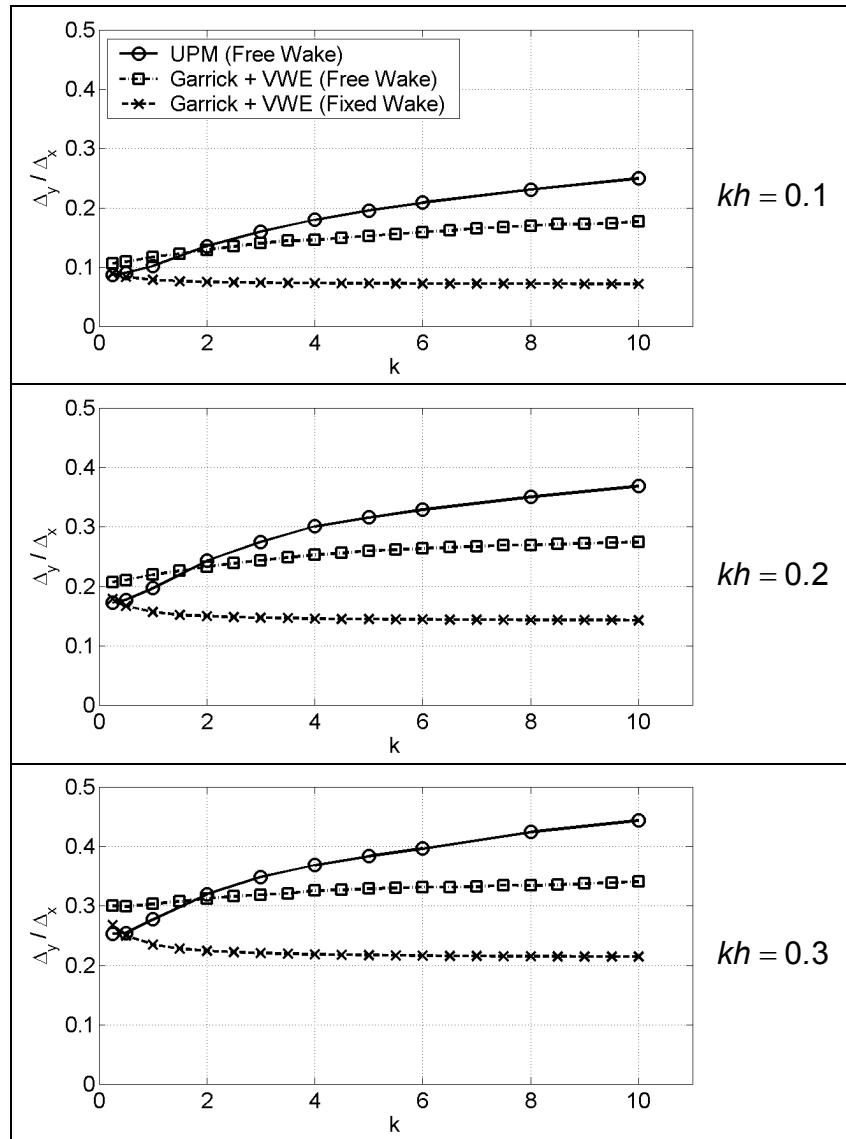


Figure 5.18. Ratio of vortex centroid spacing as a function of k and kh , UPM code (NACA0012 airfoil) and Garrick + VWE results.

The downstream tilt grows slightly more slowly with kh than for the Garrick + VWE simulations, but the growth with k is significantly more rapid. However the same basic features are observed, that is for pure plunging motion the wakes for all values of k and kh are thrust-producing with downstream-tilted vortex

pairs. In each case the vortex sheet rolls up into a single vortex per cycle of airfoil motion, with none of the variability in wake structures observed in the VWE simulations seen for example in Figure 5.2 by appropriate changes in phase. This is attributed to the Kutta condition being enforced at the trailing edge of the airfoil, resulting in the limited range of possible phases between vortex strength and airfoil motion seen in Figure 5.12.

Thus the UPM code predicts thrust-producing wakes for all values of k and h , with some variation in structure dependent on kh , but also varying with k independently.

The UPM code cannot account for viscous drag from the airfoil since it uses an inviscid (potential flow) formulation², however in reality there would be additional effects due to this drag component. If an additional viscous drag were added to the thrust predicted by the UPM model, we might expect to see drag-producing wakes at low values of k and kh , neutral wakes once k and kh were increased to the point where the thrust due to airfoil motion balanced the viscous drag, and thrust-producing wakes for further increases in k and kh .

Neither the Garrick + VWE analysis, nor the UPM code, produced vorticity distributions that gave rise to anything like the complicated multiple-vortex-pair-per-cycle structures seen in the lower frame of Figure 5.2. We would therefore expect from both the Garrick + VWE and UPM results that even in the presence of viscous drag, the sequence of wake structures in a real flow as k and kh increased would be similar to those shown in Figure 5.1 and Figure 5.3 with a single pair of vortices per cycle of airfoil motion.

² The Garrick analysis of Chapter 3 shows that a plunging flat-plate airfoil in an inviscid flow can only ever produce thrust. However a pitching airfoil may produce drag with the correct combination of frequency and pitch amplitude. This is due to the distribution of vorticity shed from the trailing edge into the wake, and is entirely separate from any additional viscous drag that would be present in a real flow.

5.3.3 Experimental Observation of Wake Structures

The wake structures behind plunging airfoils have been examined in a number of experimental and computational studies. Freymuth (1988) presented experimental flow visualisations for a NACA0015 airfoil at $Re = 5,200$ at a steady angle of attack of 5° , plunging vertically with $k = 2.7$, $h = 0.2$. The vortex wake consisted of a single pair of downstream-tilted vortices per cycle of airfoil motion, which Freymuth noted as indicating thrust production although no measurement of thrust was performed. He also stated that at very low frequencies, any thrust due to airfoil motion was overwhelmed by viscous drag and a Karman vortex street was observed.

Jones, Dohring and Platzer (1996) presented experimental visualisations for a plunging airfoil showing a drag-producing Karman street, a neutral wake with untilted vortex pairs, and a thrust-producing reverse Karman street. Their Figure 9 showed the classification of a large number of experimental wakes as drag-producing, neutral or thrust-producing based on appearance, plotted on an h -vs- k plot with a frequency range $k = 0 - 7.0$ and plunge amplitude range $h = 0 - 0.65$, for NACA0012 and NACA0015 airfoils at Reynolds numbers $Re = 500 - 100,000$. They indicated a dependence of the wake structures on kh by showing that the boundary between drag-producing and thrust-producing wakes was reasonably well represented by a line of constant kh .

Triantafyllou et al. (1993) summarised other experimental results (Ohashi and Ishikawa 1972; Kadlec and Davis 1979) for both pitching and plunging airfoils. Ohashi and Ishikawa studied a standard NACA65-010 airfoil and a modified NACA65-010 airfoil with the trailing edge radius increased from 0.0015 to 0.025 of a chord length, in a Reynolds number range $Re = 10,000 - 40,000$. The airfoils were plunged in the range $k = 0.5 - 8.5$ and $h = 0.04 - 0.45$. Kadlec and Davis studied a NACA64A006 airfoil pitching about the quarter-chord point, with a Reynolds number range of approximately $Re = 30,000 - 100,000$. The frequency range was $k = 1.0 - 10.0$, and the pitching motion gave an equivalent trailing edge motion of $h = 0.02 - 0.4$.

Figure 3 of Triantafyllou et al. is adapted here at Figure 5.19, showing regions of the h -vs- k plane giving rise to drag-producing, neutral and thrust-producing wake structures. These results indicate that the approximate boundaries separating the regions of different wake structures, determined experimentally, do not closely follow either lines of constant average thrust coefficient predicted by the Garrick model, or lines of constant kh . The difference in behaviour appears most marked for low values of h . This qualitative assessment again suggests that kh (or St) cannot be regarded as the single parameter determining the shape of the wake and the thrust developed. Rather both the reduced frequency of plunging k , and the amplitude of motion h , must be considered as separate parameters.

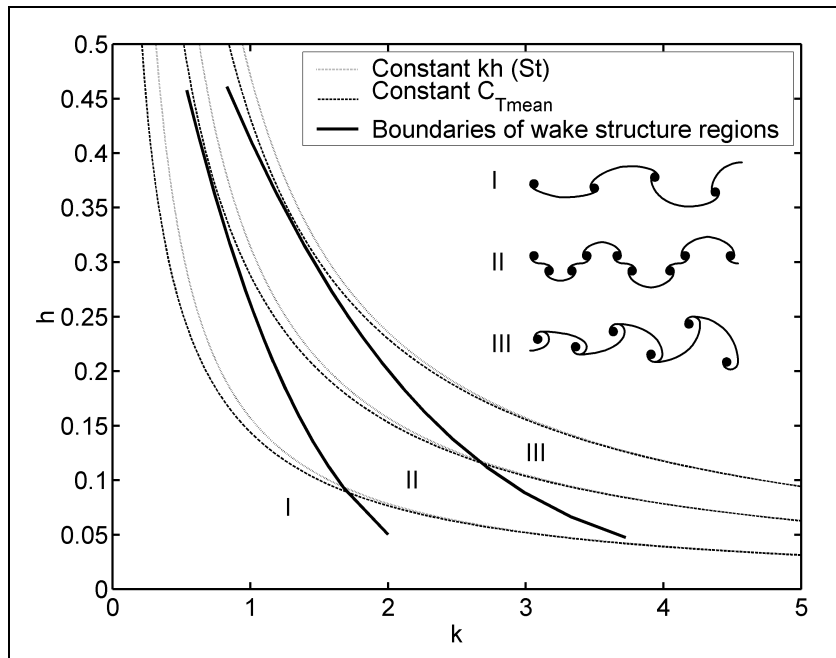


Figure 5.19. Variation of constant average thrust coefficient with k and h , predicted by Garrick theory, and experimentally derived regions of differing wake structure (Ohashi and Ishikawa 1972; Kadlec and Davis 1979; Triantafyllou et al. 1993).

Lai and Platzer (1999) also presented experimental flow visualisation of the wake of a plunging airfoil. They studied a NACA0012 airfoil at a Reynolds number $Re = 20,000$, plunging vertically in the range approximately $k = 0 - 60$ and $kh = 0 - 4.65$. Note that this very large range of kh corresponds to angles of attack due to the plunging motion of $\alpha_{\text{plunge}} = \tan^{-1}(2kh) = 0 - 84^\circ$. They

provided a number of wake visualisations showing drag-producing, neutral and thrust-producing wake structures such as those of Figure 5.1 and Figure 5.3, and interestingly some showing more complicated structures with multiple vortices shed per half-cycle of motion, similar to that produced in the lower frame of Figure 5.2.

Figure 5.20 to Figure 5.23 are reproduced from Lai and Platzer (1999). Dye was released into the flow from the airfoil close to the trailing edge (red from the upper surface, green from the lower). Flow is from left to right in each figure. Note that the background of each figure has been processed to bring out details of the wake.

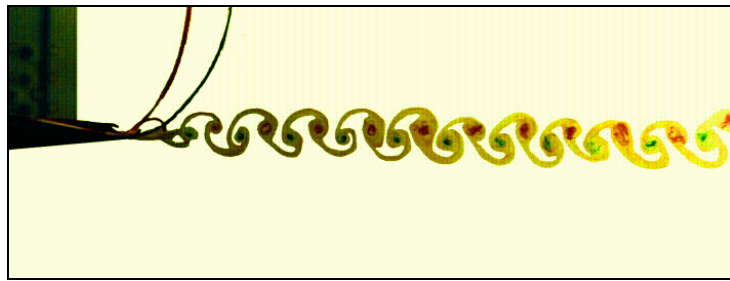


Figure 5.20. Stationary NACA0012 airfoil at $Re = 20,000$ showing Karman vortex street due to ‘natural vortex shedding’ (Lai and Platzer 1999).

Figure 5.20 shows the wake of a stationary NACA0012 airfoil at $Re = 20,000$. At this low Reynolds number the airfoil, even though streamlined, acts somewhat like a bluff body. Vortices are shed alternately from either side of the trailing edge in a manner analogous to the shedding behind a circular cylinder or other bluff bodies. The vortex pairs consisting of one red (clockwise vorticity) and one green (anti-clockwise vorticity) are clearly tilted upstream, indicative of the viscous drag of the airfoil. The overall wake structure is similar to that produced in the upper frame of Figure 5.1. This shedding mode is hereafter referred to as ‘natural shedding’, as opposed to the ‘forced shedding’ induced by the motion of the airfoil.

Figure 5.21 shows a sequence of wake structures at a given frequency, increasing the plunge amplitude h , thus increasing kh . From previous Garrick + VWE and UPM results we might expect that increasing kh would involve a

change from drag-producing, through neutral, to thrust-producing wakes. This is observed, in that pairs of opposite vorticity (red and green dye) are tilted upstream in (a), untilted in (b), and tilted downstream in (c) and (d). However the two upper frames show two pairs of vortices shed from the trailing edge per cycle of airfoil motion, rather than the single pair seen in the two lower frames.

These multiple-vortex-pair-per-cycle types of structures were also drawn schematically in the wake classification diagram of Ohashi and Ishikawa (1972), adapted in Figure 5.19.

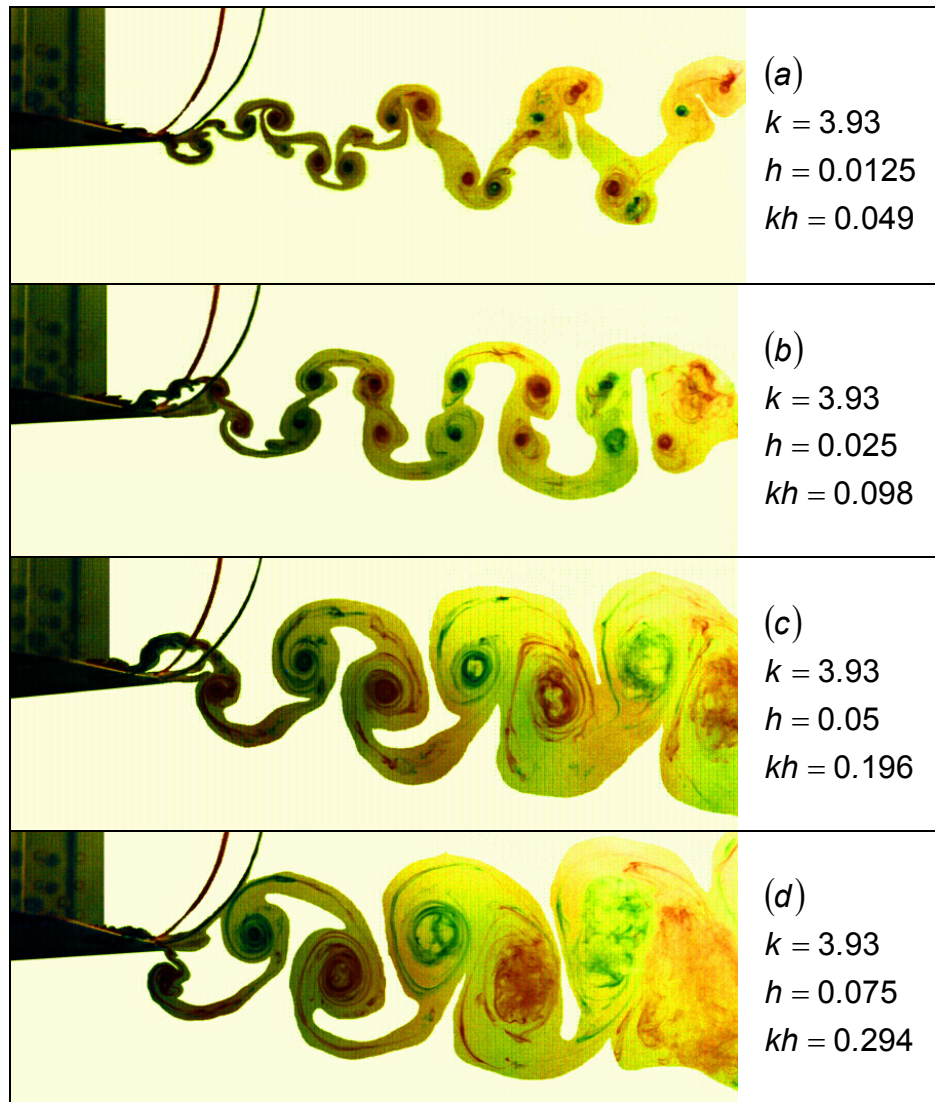


Figure 5.21. NACA0012 airfoil at $Re = 20,000$ showing change from drag-producing (a), to neutral (b) and thrust producing (c,d) wake structures, from Lai and Platzer (1999).

Figure 5.22 shows the same four plunging amplitudes as Figure 5.21, but with the frequency doubled, thus doubling kh in each case. We now see only a single vortex pair shed per cycle of airfoil motion, in each of the frames. The lowest kh , frame (a), appears to have very slightly upstream-titled vortices indicating a slight net drag, quite close to a neutral wake. The other frames show clearly thrust-producing wakes.

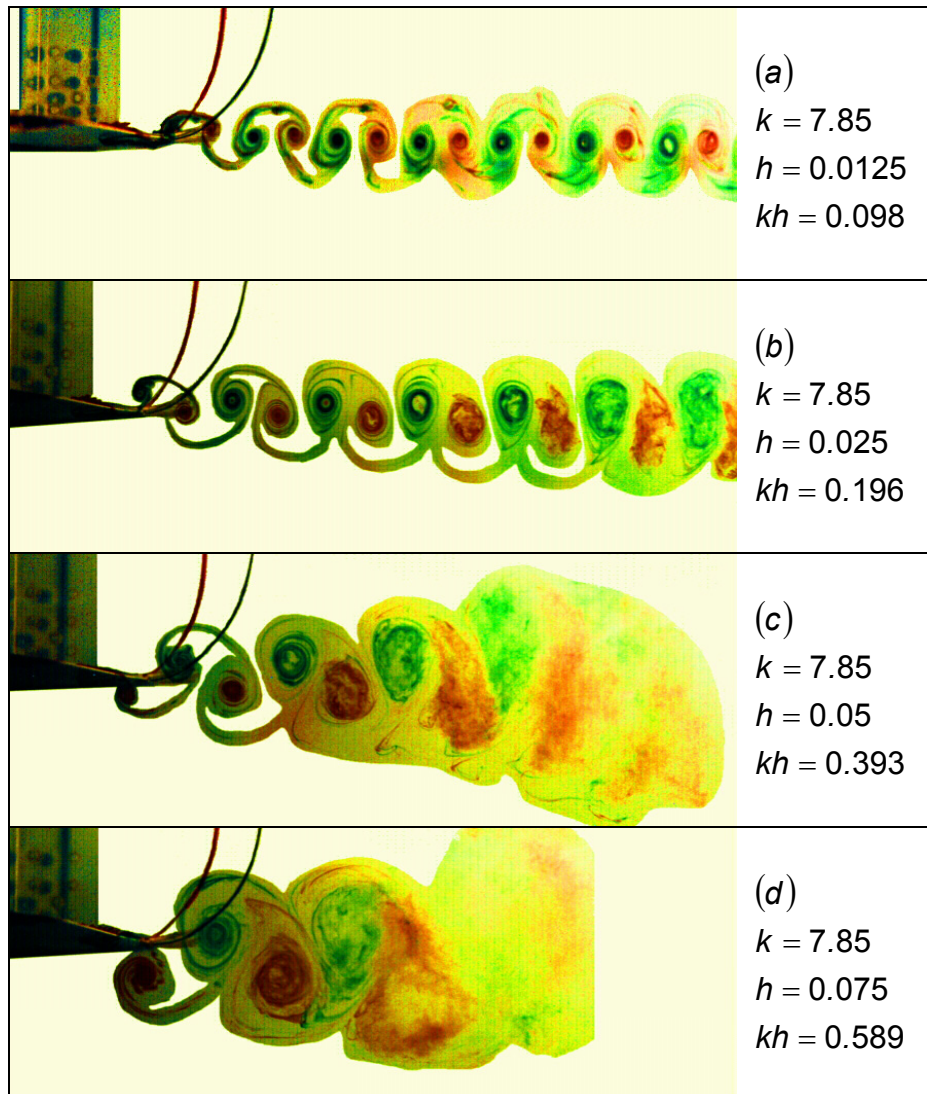


Figure 5.22. NACA0012 airfoil at $Re = 20,000$, at twice the frequency of Figure 5.21, from Lai and Platzer (1999).

Figure 5.23 shows the same runs, with the frequency again doubled. Now the wake structures are quite different again, with one pair of vortices shed per cycle of airfoil motion, tilted downstream indicating thrust in each case. Here

though the wake is asymmetric about the centreline of the motion, in a manner reported elsewhere (Jones et al. 1996; 1998).

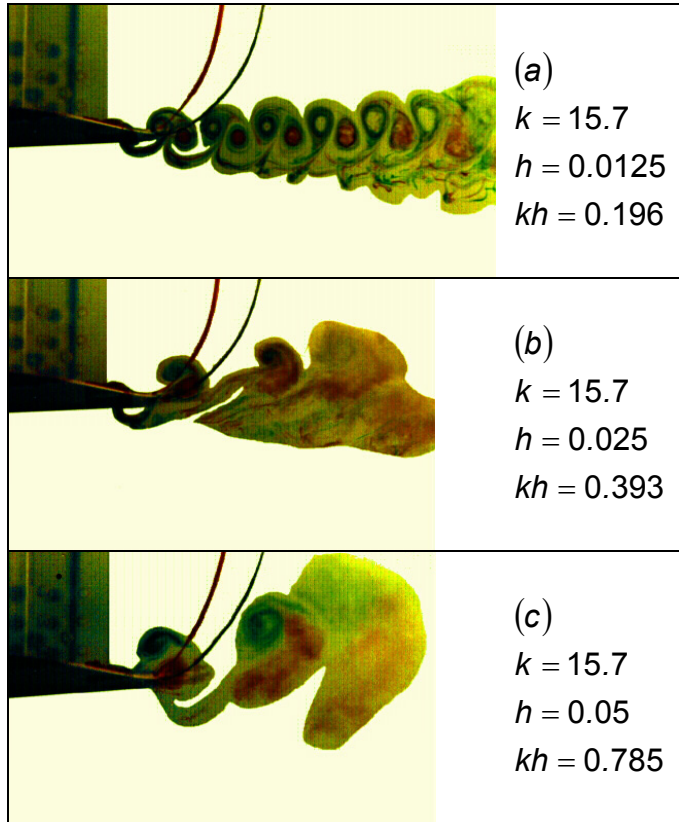


Figure 5.23. NACA0012 airfoil at $Re = 20,000$, at four times the frequency of Figure 5.21, from Lai and Platzer (1999).

Comparison of Figure 5.21 to Figure 5.23 shows that runs at the same kh do not necessarily produce geometrically equivalent wake structures. Figure 5.21 (c), Figure 5.22 (b) and Figure 5.23 (a) are all at the same kh but different k , and show some small variation in wake shape. Figure 5.21 (b) and Figure 5.22 (a) are both at the same kh but show very different wake structures even though both appear to be close to neutral wakes. This clearly indicates that at these flow conditions and plunging parameter ranges, kh cannot be the single parameter controlling the shedding of vorticity into the wake, but that there is also an effect due to frequency k . It is interesting to note that this variability with k and kh is quite different to that predicted by the Garrick + VWE and UPM codes, and that the variability is much more pronounced than predicted by either of those methods.

In attempting to determine the origin of the multiple-vortex-pair-per-cycle shedding, it is useful to examine a hierarchy of methods from the linearised potential flow analysis, through the UPM code to the Navier-Stokes (NS) solver.

The Garrick linearised analysis utilises potential flow, so that the flow is inviscid and incompressible. The Kutta condition is enforced, ensuring that flow leaves the trailing edge smoothly and tangentially, and there is no flow separation from any point on the (flat plate) airfoil. The wake is assumed to be ‘frozen’, in that it maintains its shape as it is convected downstream at the free-stream velocity. The effect of non-linear self-induced wake roll-up on likely wake structures can be partially accounted for with the addition of the VWE code using the Garrick sinusoidal-strength wake as an input, which results in both wake evolution and an effective wake convection velocity higher than the free-stream.

The UPM code adds some additional realism, in that a finite thickness airfoil is simulated. The wake roll-up is also more fully accounted for in that the rolled-up wake modifies the airflow over the wing and vice-versa, slightly altering the phase between vorticity shedding and airfoil motion. However the flow is still considered inviscid and incompressible and the Kutta condition is still enforced at the trailing edge, so that no separation is allowed anywhere on the airfoil surface.

The NS code includes the effects of a finite thickness airfoil and non-linear wake evolution. However the flow is treated as viscous, and the Kutta condition is not explicitly enforced, so that flow separation effects become possible. It also includes the possibility of representing the flow as laminar or turbulent, through the use of turbulence models. The NS code thus represents the ‘full’ physics of the flow (at least as far as 2D flow is concerned). Comparison of the results from the Garrick, UPM and NS methods can be used to assess the role of these elements in the shedding phenomena observed in Figure 5.21 and Figure 5.22.

5.3.4 Navier-Stokes (NS) Solver Wake Structures

As set out in Chapter 4, the NS code is able to closely match the natural shedding frequency of a NACA0012 airfoil at a Reynolds number $Re = 12,000$. When the code was applied at $Re = 20,000$, it produced the wake structure shown in Figure 5.24, compared with a close-up of Figure 5.20. Here filled contours of entropy (p/ρ^γ) are plotted.

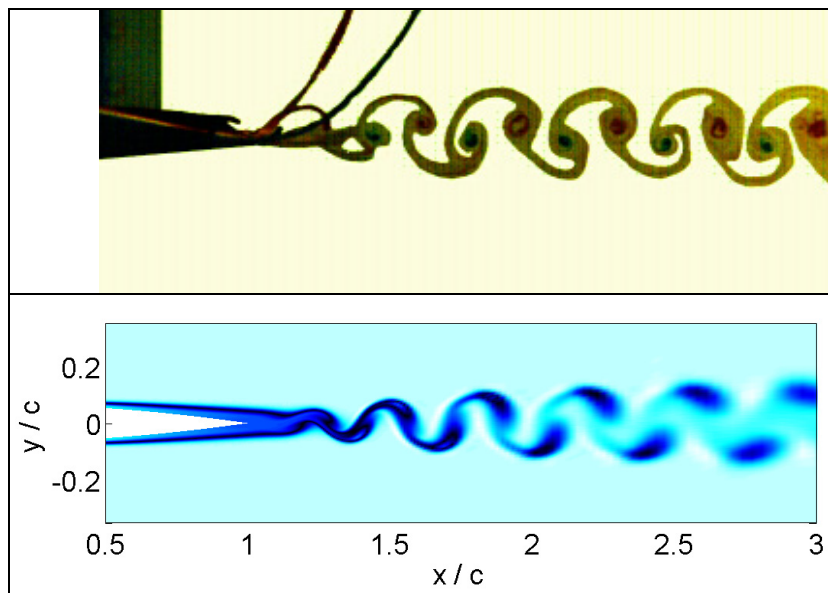


Figure 5.24. Natural shedding of a NACA0012 airfoil at $Re = 20,000$, Lai and Platzer (1999) experiment, and NS calculation ($M_\infty = 0.05$, laminar).

The details of the wake structure appear to be accurately reproduced by the NS code. The frequency of the shedding was not measured in the experiment, however the NS code produced a natural shedding frequency of approximately $k = 9.4$ at $Re = 20,000$. Based on the good agreement between experiment and calculation at $Re = 12,000$, this result is likely to be reasonably accurate.

The NS code was also able to closely reproduce the wake structures seen in the Lai and Platzer (1999) experiment, across a range of plunging frequencies and amplitudes. Numerical results were generated at a free-stream Mach number $M_\infty = 0.05$, assuming either fully laminar or fully turbulent flow. Scalar particles representing the dye in the experiments were released from a vertical plane (a ‘rake’) at the trailing edge of the airfoil, that moved with the airfoil. Red

particles were released from the upper half of the rake, and green from the lower half. In this way clockwise vorticity shed from the upper surface of the airfoil is seen in the following flow visualisations as red, and anti-clockwise vorticity shed from the lower surface as green, mimicking the experimental setup.

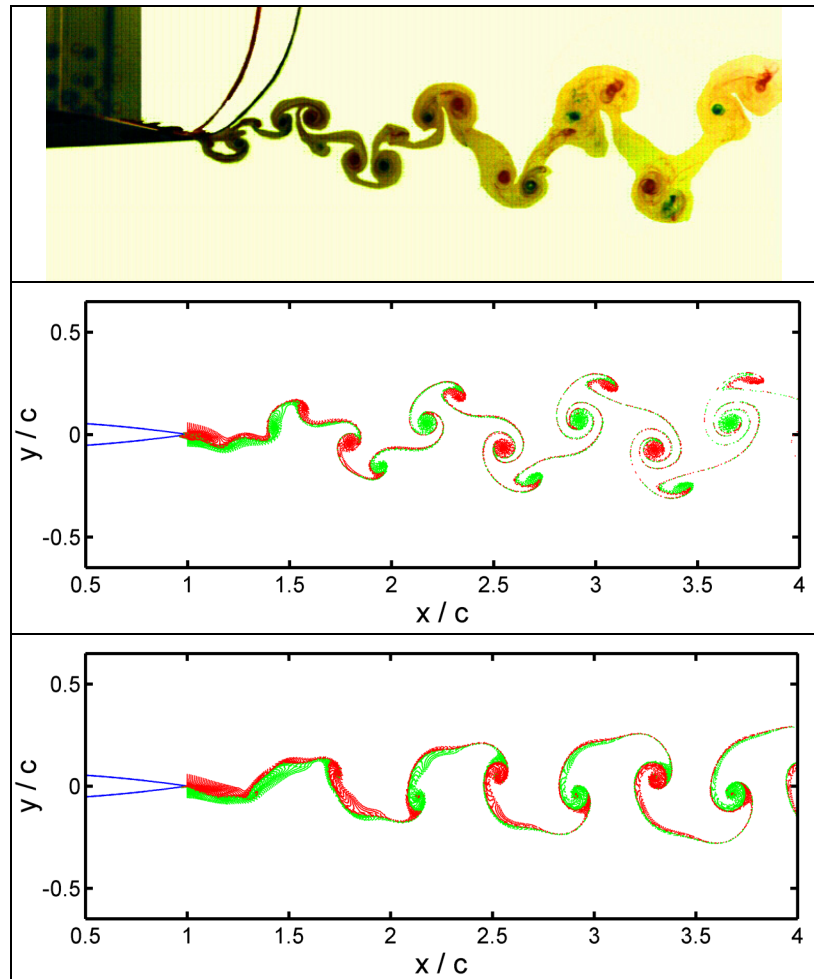


Figure 5.25. Wake comparison, $Re = 20,000$, experimental $k = 3.93$, $h = 0.0125$ (upper), NS $k = 4.0$, $h = 0.0125$, $M_\infty = 0.05$, laminar (middle) and turbulent (lower).

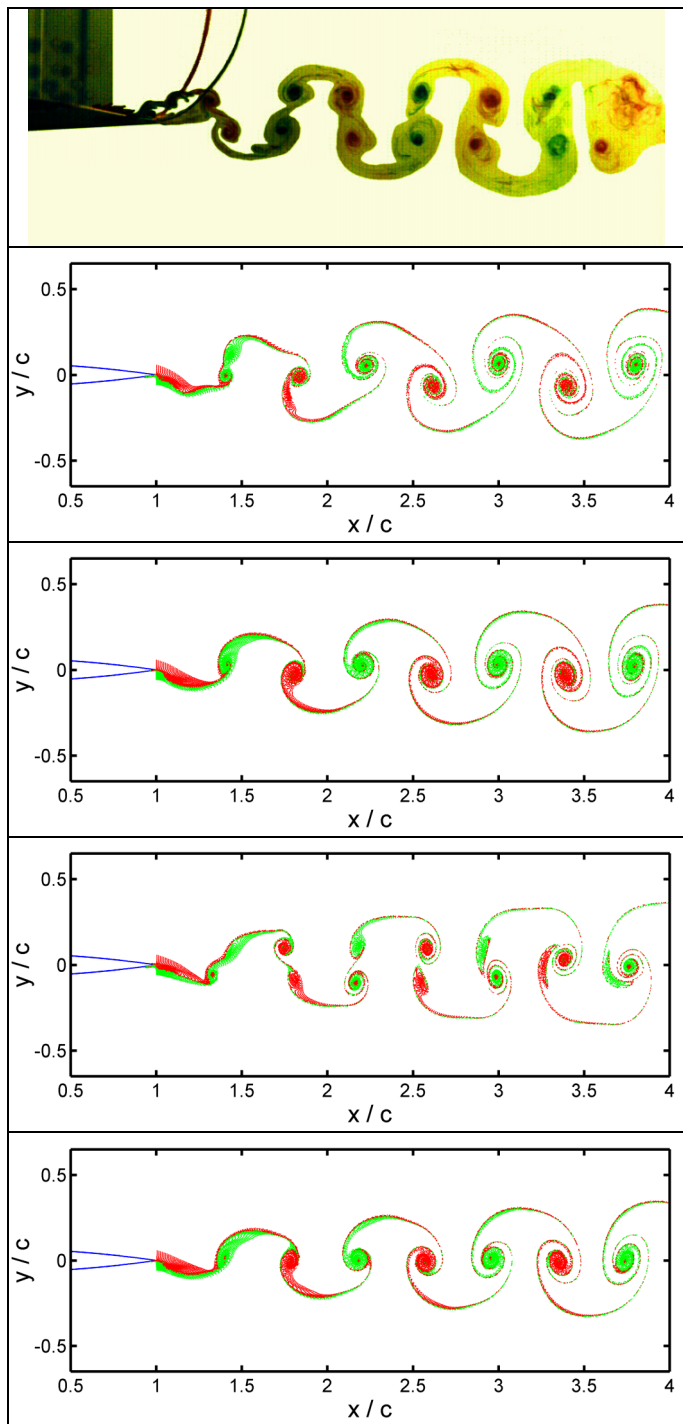


Figure 5.26. Wake comparison, $Re = 20,000$, experimental $k = 3.93$, $h = 0.025$ (first frame), NS $k = 4.0$, $h = 0.025$, $M_\infty = 0.05$, laminar and turbulent (second and third frames), NS $k = 4.0$, $h = 0.02$, laminar and turbulent (fourth and fifth frames).

Figure 5.25 compares experimental and numerical results at $k \approx 4.0$ and $h = 0.0125$. The fully laminar numerical results reproduce the same qualitative aspects of the experimental wake vortex structure, with two roughly equal strength same-sign vortices shed per half-cycle of airfoil motion, and upstream-tilted vortex pairs indicative of net drag (confirmed by averaged flow field calculations showing a momentum-deficit wake aft of the trailing edge, not presented here). The fully turbulent numerical results are qualitatively different, and although there are still two same-sign vortices shed per half-cycle, they are now of different strength and the wake dynamics are quite dissimilar. Here the smaller vortices are stretched by the induced velocity of the larger vortex pairs, resulting in what appears much more like a Karman vortex street (but again with upstream-tilted vortex pairs indicative of drag). For this combination of k and h , the fully laminar results are clearly the better match for the observed wake.

Figure 5.26 compares experimental results at $k \approx 4.0$, $h = 0.025$, and numerical results at $k = 4.0$, $h = 0.025$ and $k = 4.0$, $h = 0.02$. The experimental results show a neutral wake, where the thrust developed by the airfoil motion is balanced by the inherent drag, resulting in no net thrust, and untilted vortex pairs. Here again we see a marked difference in the numerical results between fully laminar and fully turbulent cases in the overall shape of the wake. The laminar results clearly show two same-sign vortices shed per half cycle of airfoil motion, whereas the turbulent results have the same form as for $h = 0.0125$ where the second same-sign vortex is greatly reduced in size, and stretched by the action of the larger vortices. The laminar numerical results at $h = 0.02$ are a better match for the experimental visualization than at $h = 0.025$; they show similar position and relative size of shed vortices, as well as similar wake dynamics in that vortex pairs start to move through one another via self-induced velocities. The experimental behaviour has been reproduced qualitatively in that a neutral wake is produced, although at a lower oscillation amplitude than in the experiment. Similar results were observed for calculations made at both $M_\infty = 0.05$ and $M_\infty = 0.2$, with different levels of grid refinement.

Figure 5.27 compares experimental and numerical results at $k \approx 4.0$ and $h = 0.05$. For both the laminar and turbulent numerical results, a close similarity

with the experimental visualization is apparent in terms of the large scale shape of the wake, with downstream-tilted vortex pairs indicative of net thrust (confirmed by averaged flow field calculations showing a jet aft of the trailing edge, not presented here). For this case, little difference between laminar and turbulent results is discernable.

Figure 5.28 compares experimental and numerical results at $k \approx 4.0$ and $h = 0.075$. Again a close large-scale similarity with the experimental visualization is apparent for both laminar and turbulent numerical results. Helmholtz shear-layer instability vortices are visible in between the large shed vortices. Fully turbulent numerical results are very similar on the large scale, but the shear-layer instability is not as prominent.

Figure 5.29 compares experimental and numerical results at $k \approx 8.0$, $h = 0.0125$. The macroscopic wake structure is well approximated by both the laminar and turbulent numerical results. Contrasting these figures to the results in Figure 5.26, produced at half the reduced frequency but with the same value of kh , we see a marked difference in the wake structure.

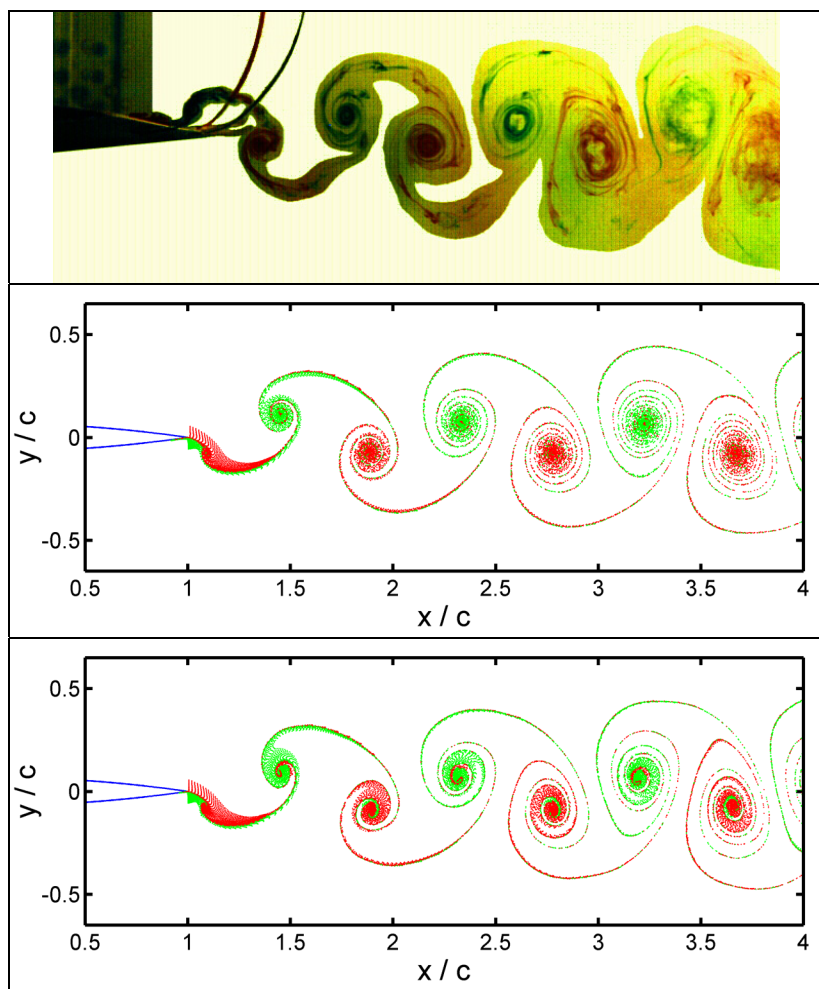


Figure 5.27. Wake comparison, experimental $k = 3.93$, $h = 0.05$ (upper), NS $k = 4.0$, $h = 0.05$, laminar (middle) and turbulent (lower).

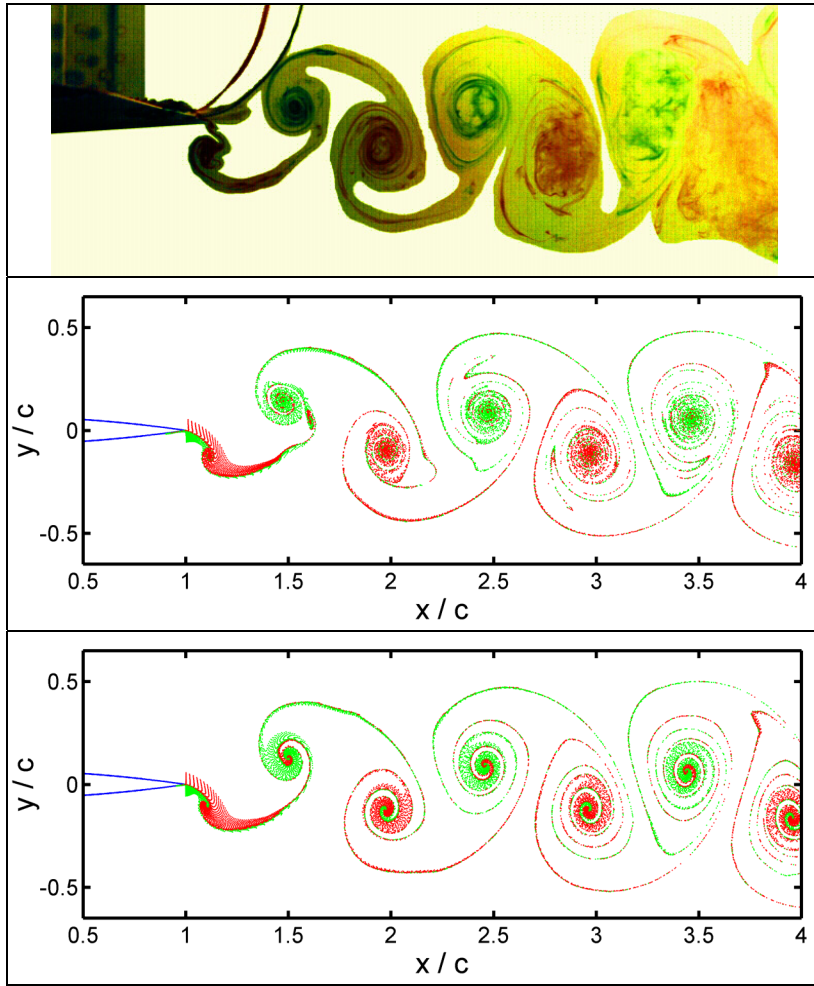


Figure 5.28. Wake comparison, experimental $k = 3.93$, $h = 0.075$ (upper), NS $k = 4.0$, $h = 0.075$, laminar (middle) and turbulent (lower).

The results presented in Figure 5.25 to Figure 5.29 show very good agreement between the computational results of the NS code and the experimental results of Lai and Platzer (1999). They also compare well to other experimental wake visualizations in the literature (Ohashi and Ishikawa 1972; Kadlec and Davis 1979). The agreement between the experimental and numerical laminar results at the lower plunge amplitudes is more likely to be an indication that the flow in the experiments of Lai and Platzer was laminar, than that the turbulence model is doing a poor job of predicting the flow. Convergence of laminar and turbulent results for larger amplitudes is discussed in Section 5.5.

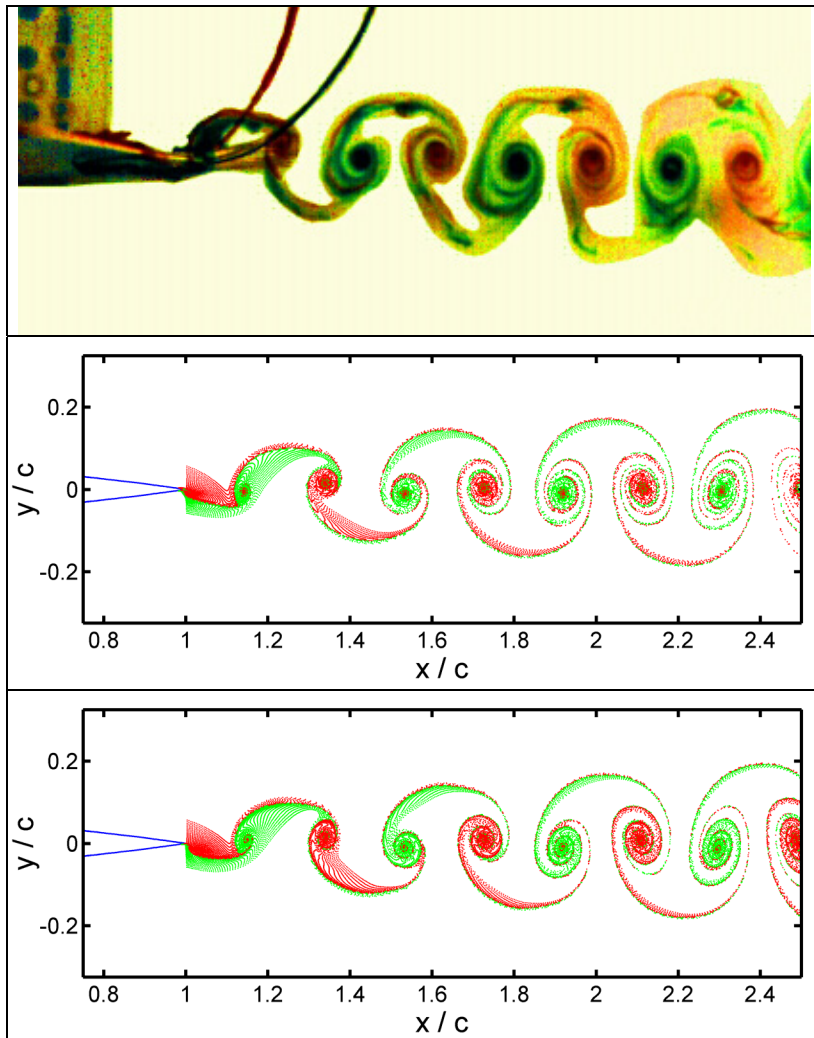


Figure 5.29. Wake comparison, experimental $k = 7.85$, $h = 0.0125$ (upper), Numerical $k = 8.0$, $h = 0.0125$, laminar (middle) and turbulent (lower).

Having achieved very good agreement between the NS code results and experiments, the NS code can now be used to further explore the relationship between observed wake structures and the plunge motion frequency and amplitude.

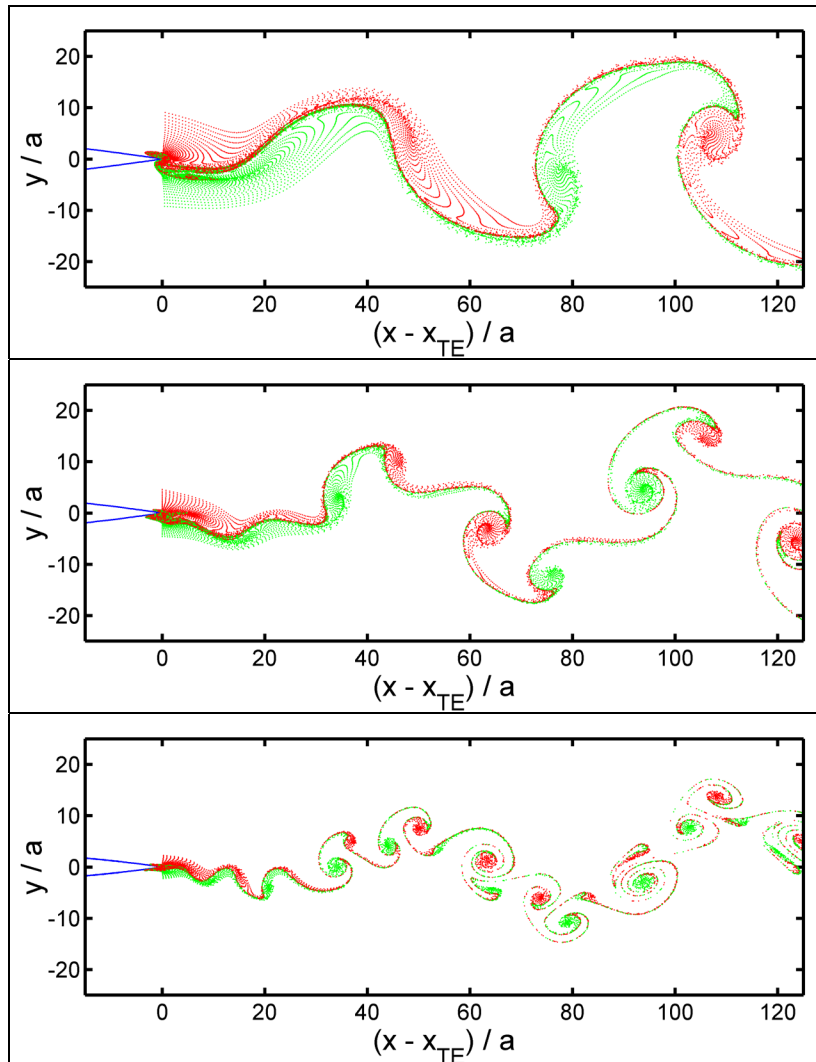


Figure 5.30. NS laminar, $kh = 0.05$: $k = 8.0, h = 0.00625$ (upper), $k = 4.0, h = 0.0125$ (middle), $k = 2.0, h = 0.025$ (lower).

Figure 5.30 compares three numerical laminar wakes produced at $kh = 0.05$, but with varying k and h . The wakes are shown at the same equivalent scale (normalized against plunge amplitude $a = hc$). We see a straightforward Karman vortex street at $k = 8.0, h = 0.00625$, but much more complicated multiple-vortex-pair-per-cycle type shedding at $k = 4.0, h = 0.0125$ and $k = 2.0, h = 0.025$.

The equivalent wake structures, calculated with the UPM code for the same plunging parameters, are shown in Figure 5.31. Here the strength of each individual wake vortex is represented by its relative size.

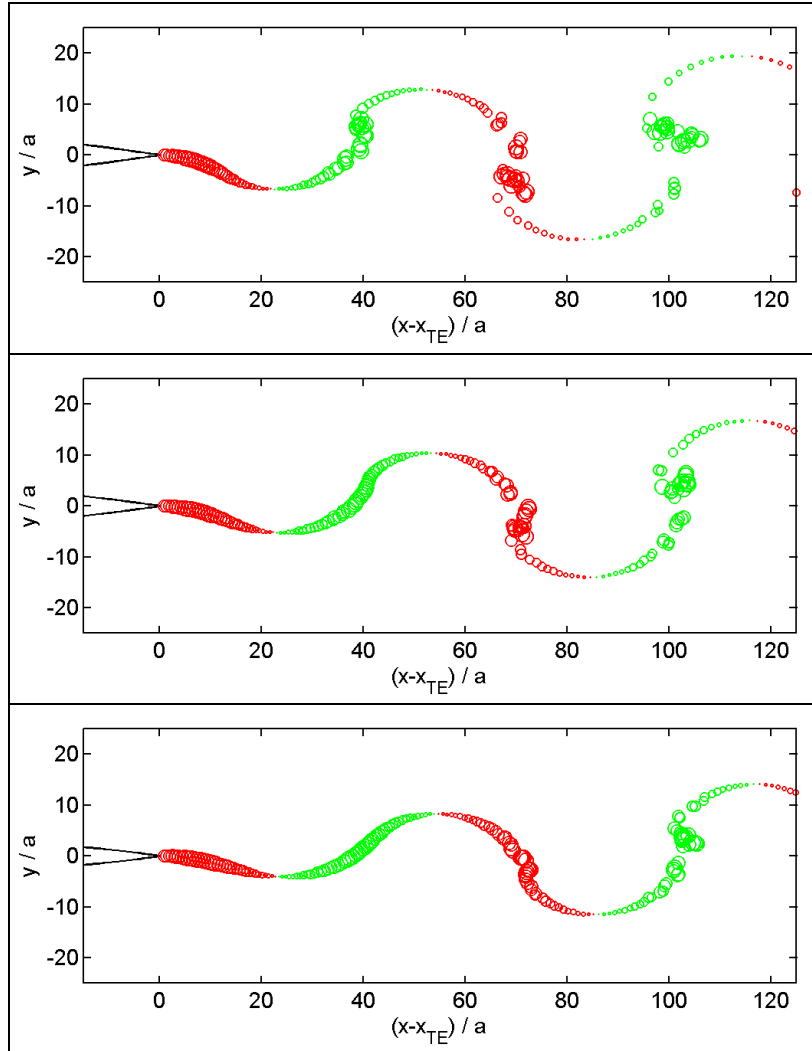


Figure 5.31. UPM wake structures, $kh = 0.05$: $k = 8.0, h = 0.00625$ (upper), $k = 4.0, h = 0.0125$ (middle), $k = 2.0, h = 0.025$ (lower).

The UPM code is unable to reproduce the multiple-vortex-pair-per-cycle shedding in the NS code results.

Figure 5.32 shows the same plunging frequencies but with $kh = 0.1$, and again there is a marked difference in wake structures. In these figures the normalized wavelength of the wake remains approximately the same as k is varied, but the distribution of vorticity shed into the wake throughout the plunge cycle varies significantly.

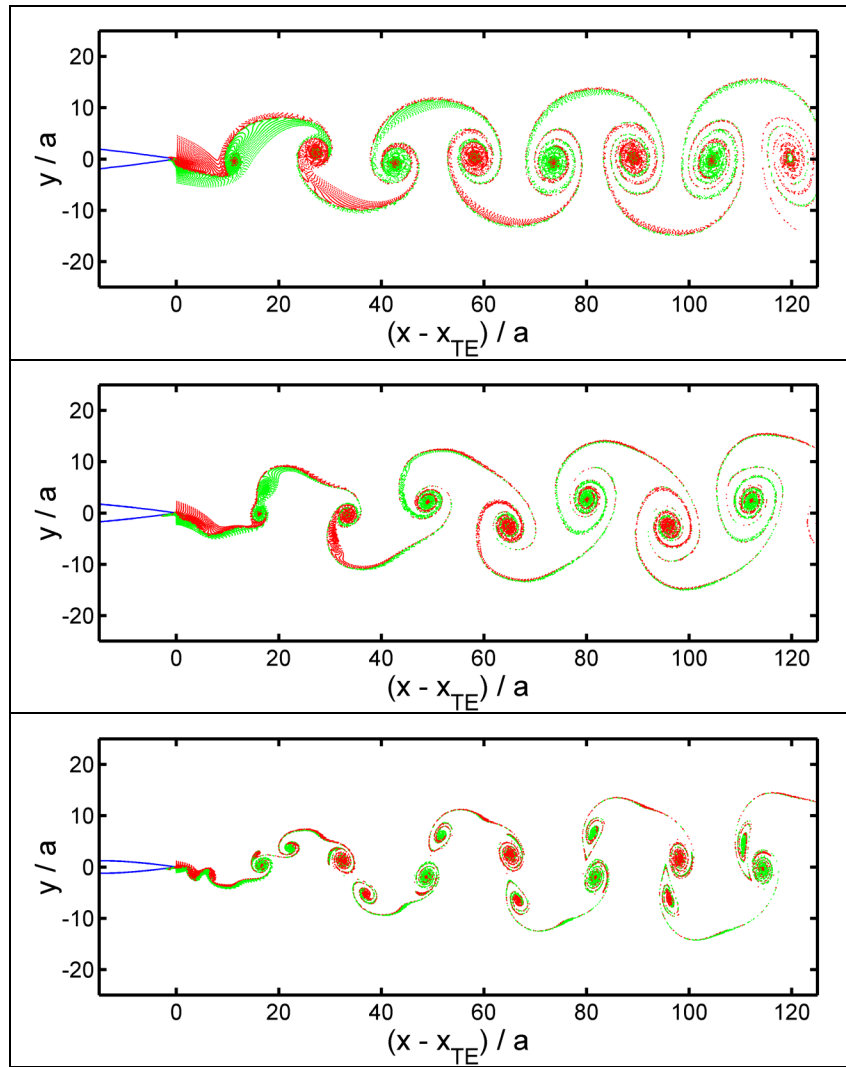


Figure 5.32. NS laminar, $kh = 0.1$: $k = 8.0, h = 0.0125$ (upper), $k = 4.0, h = 0.025$ (middle), $k = 2.0, h = 0.05$ (lower).

Figure 5.33 shows the equivalent wake structures, calculated with the UPM code for the same plunging parameters as Figure 5.32.

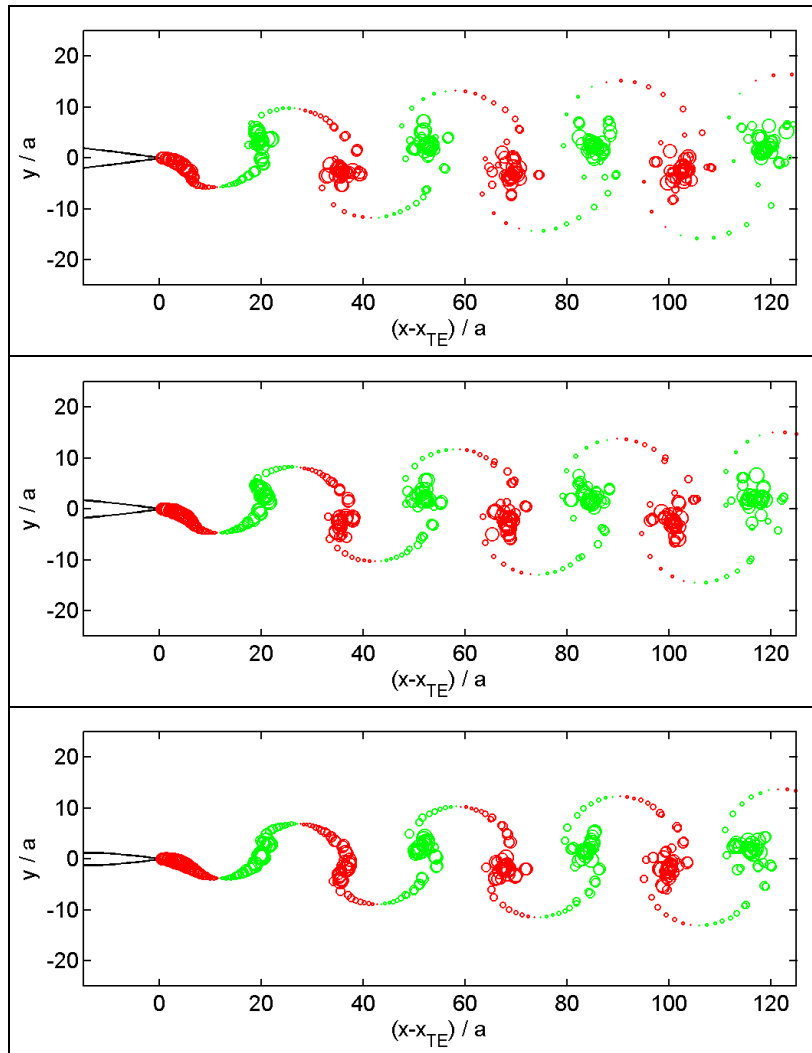


Figure 5.33. UPM $kh = 0.1$: $k = 8.0, h = 0.0125$ (upper), $k = 4.0, h = 0.025$ (middle), $k = 2.0, h = 0.05$ (lower).

Again, the UPM code is unable to reproduce the complicated wake structures of the NS code results.

Figure 5.30 and Figure 5.32 provide further evidence that kh is not the sole parameter controlling the observed wake structures, but rather that there is an additional effect due to frequency k . The fact that the UPM code is unable to reproduce the observed shedding phenomena seen in both experimental visualisations and NS code results, and the differences in simulated physics between the NS and UPM codes, implies that the multiple-vortex-pair-per-cycle shedding is due to viscous effects.

Similar wake vortex behaviour was simulated using the VWE code (see Figure 5.2 lower frame) as a result of an appropriate phase difference between the strength of the shed vorticity and the airfoil motion. In the VWE simulations this phase difference was arbitrarily imposed. Both the Garrick + VWE and UPM simulations, where the phase difference was determined by the Kutta condition, were unable to reproduce this wake behaviour. Thus in the real flow the phase difference must be attributed to some other cause. In particular flow separation from the leading and trailing edges of the airfoil, the influence of natural shedding, and the validity of the Kutta condition must all be examined.

5.4 Multiple Vortex Pair Shedding Modes and Vortex Lock-In

Leading edge shedding may immediately be dismissed as a source of the multiple-vortex-per-half-cycle shedding evident in Figure 5.25. By skipping ahead to Figure 5.40, which shows the flow around the entire airfoil for $k = 4.0$, $h = 0.25$, $Re = 20,000$ in the second frame, one may see that there is no evidence of any leading edge vortices at these conditions.

The presence of a natural shedding frequency due to trailing edge separation for the airfoil in the Reynolds number range under investigation, in addition to the forced frequency imposed by the airfoil motion, leads to the possibility of interaction between the two frequencies.

Figure 5.34 provides a close-up on the trailing edge at one instant in the plunge cycle, for $k = 4.0$, $h = 0.0125$, fully laminar flow, showing instantaneous streamlines and the corresponding scalar particle trace. Animations of the flow structure at the trailing edge throughout the plunge cycle show separation

regions on either or both sides of the airfoil, around which the remainder of the fluid flows, creating an effectively blunt-edged body. This may be seen in Figure 5.34, where the streamlines at the trailing edge flow around a region of separated flow rather than the sharp trailing edge itself.

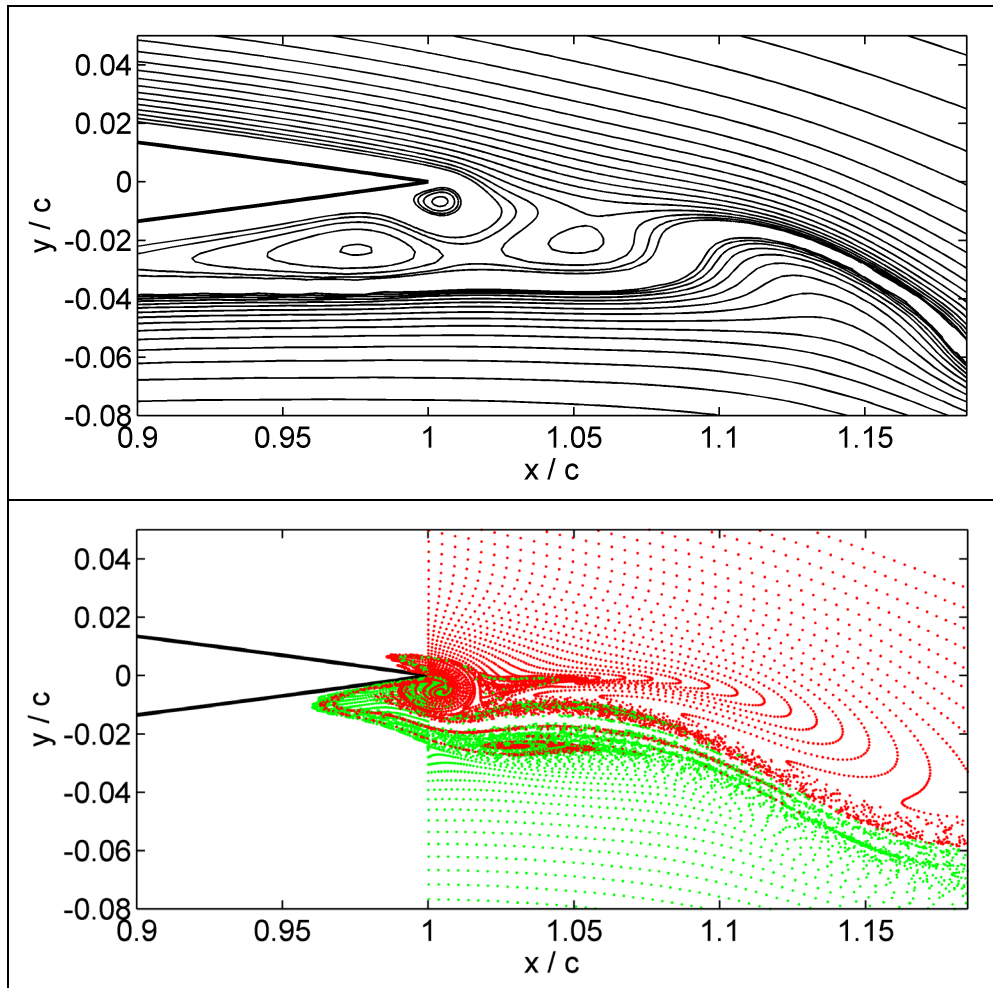


Figure 5.34. Instantaneous streamlines (contours of stream function calculated from velocity field relative to the airfoil, contour values chosen on a log scale to bring out detail) and the corresponding particle trace snapshot, numerical laminar $k = 4.0$, $h = 0.0125$, $Re = 20,000$, airfoil moving upwards through the centreline of motion.

The degree of effective bluntness of the airfoil trailing edge varies throughout the plunge cycle, as well as with k and h . The trailing edge of the airfoil, now acting as a bluff body, will have a natural shedding frequency associated with it which will vary somewhat with the Reynolds number (see e.g. Hannemann and Oertel 1989 showing natural shedding for a flat plate of finite thickness, end-on

to the flow). Interaction of this natural shedding mode with the vortex shedding associated with the airfoil plunge frequency appears to be the origin of the multiple-vortex-per-half-cycle shedding apparent in Figure 5.30 and Figure 5.32.

Such interaction between natural shedding and forced frequencies has been observed in the vibration of circular cylinders and other bluff bodies. Karniadakis and Triantafyllou (1989) studied the wake of a cylinder in laminar flow using a spectral elements Navier-Stokes solver. They noted the experimental results of Koopman (1967) showing that below a certain amplitude of forced transverse vibration, only the natural shedding frequency is apparent in the wake of the cylinder. Above the threshold forcing amplitude the forcing frequency becomes visible in the wake structures.

Karniadakis and Triantafyllou used a numerical forcing function in the wake, consisting of a local additional acceleration, to simulate the effect of an active control device such as a thin vibrating wire. They showed that on a graph of forcing amplitude versus forcing frequency, the wake can select one of three possible states. Inside a roughly parabolic region of the graph centred on the natural shedding frequency and above a threshold amplitude, the wake oscillates periodically at the forced frequency. This is known as the ‘vortex lock-in’ region, and the boundary as the ‘lock-in boundary’. Outside this region, there is a ‘receptivity boundary’ inside which there is interaction between the forced and natural frequencies leading to quasi-periodic and non-period (chaotic) vortex shedding. Outside the receptivity boundary, the wake oscillates periodically at the natural shedding frequency. This is illustrated schematically in Figure 5.35.

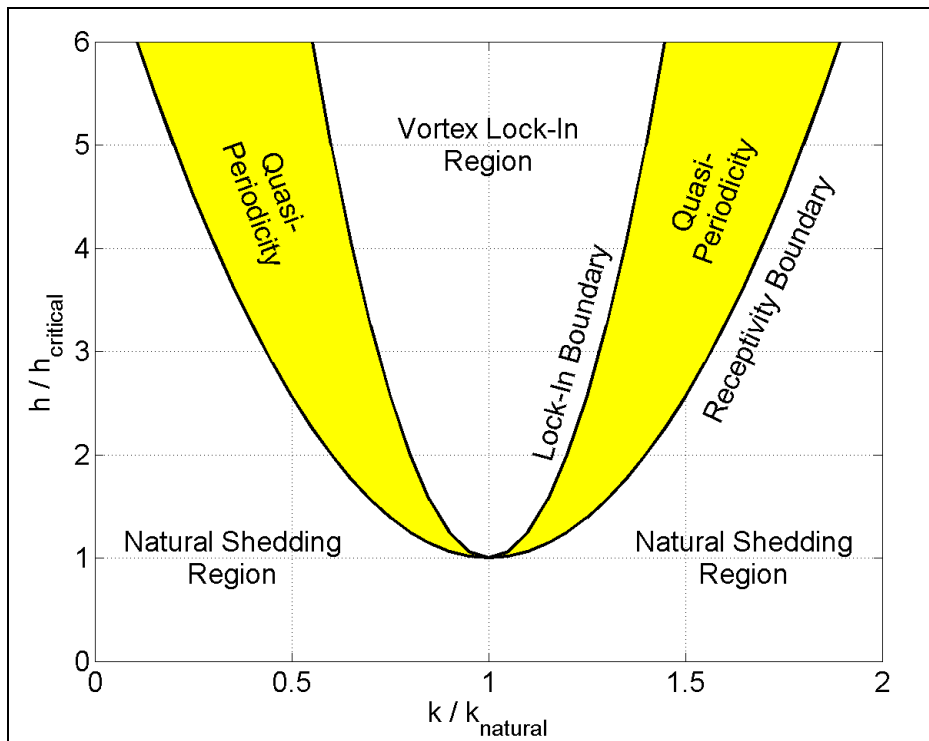


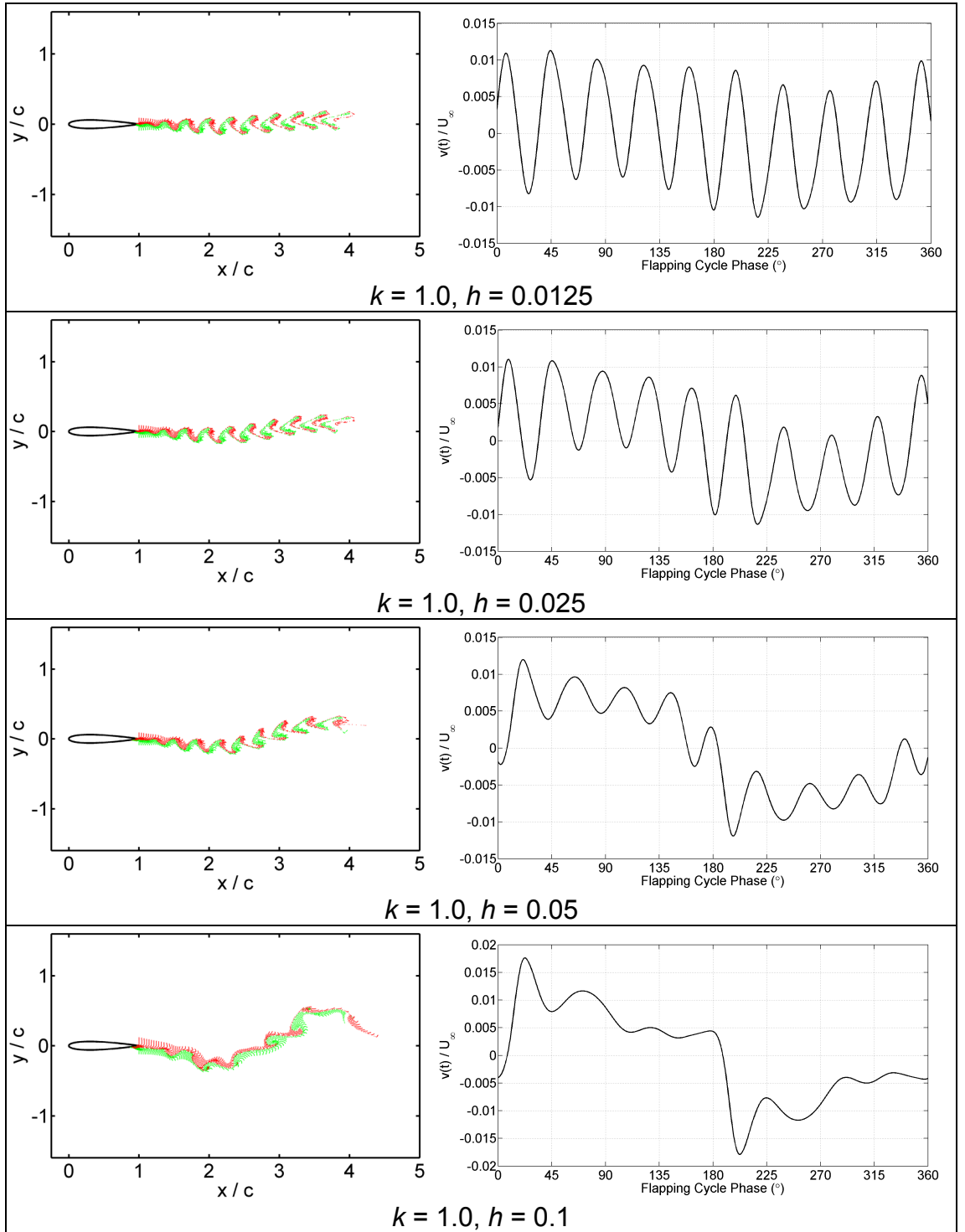
Figure 5.35. Schematic vortex lock-in boundary for a circular cylinder, after Karniadakis and Triantafyllou (1989).

Patnaik, Narayana and Seetharamu (1999) examined the laminar flow past a transversely vibrating cylinder using a finite elements Navier-Stokes solver. Here the forcing is due to the motion of the cylinder, rather than any control device in the wake. They calculated an approximate lock-in boundary, and found it to be roughly of the shape stated in Karniadakis and Triantafyllou (1989), and as found by other researchers.

It is reasonable to expect that a similar phenomenon may manifest itself in the wake of the plunging airfoil, although the different geometry may give rise to a different lock-in boundary shape. This possibility is investigated below.

Figure 5.36 shows a series of particle traces (left frames) generated with reduced frequency held constant at $k = 1.0$, and plunge amplitude h varied from 0.0125 to 0.5. The right frames show the vertical velocity measured in the wake throughout the plunging cycle, at a fixed point in the wake on the centreline of the motion, half a chord-length downstream of the trailing edge. The natural shedding frequency is apparent in the first three particle traces ($h = 0.0125$ to 0.05), and the corresponding velocity time histories are dominated by the

natural shedding. Note that the shedding frequency is not an integral multiple of the plunging frequency, so the velocity time histories do not have equal values at the beginning and end of the flapping cycle.



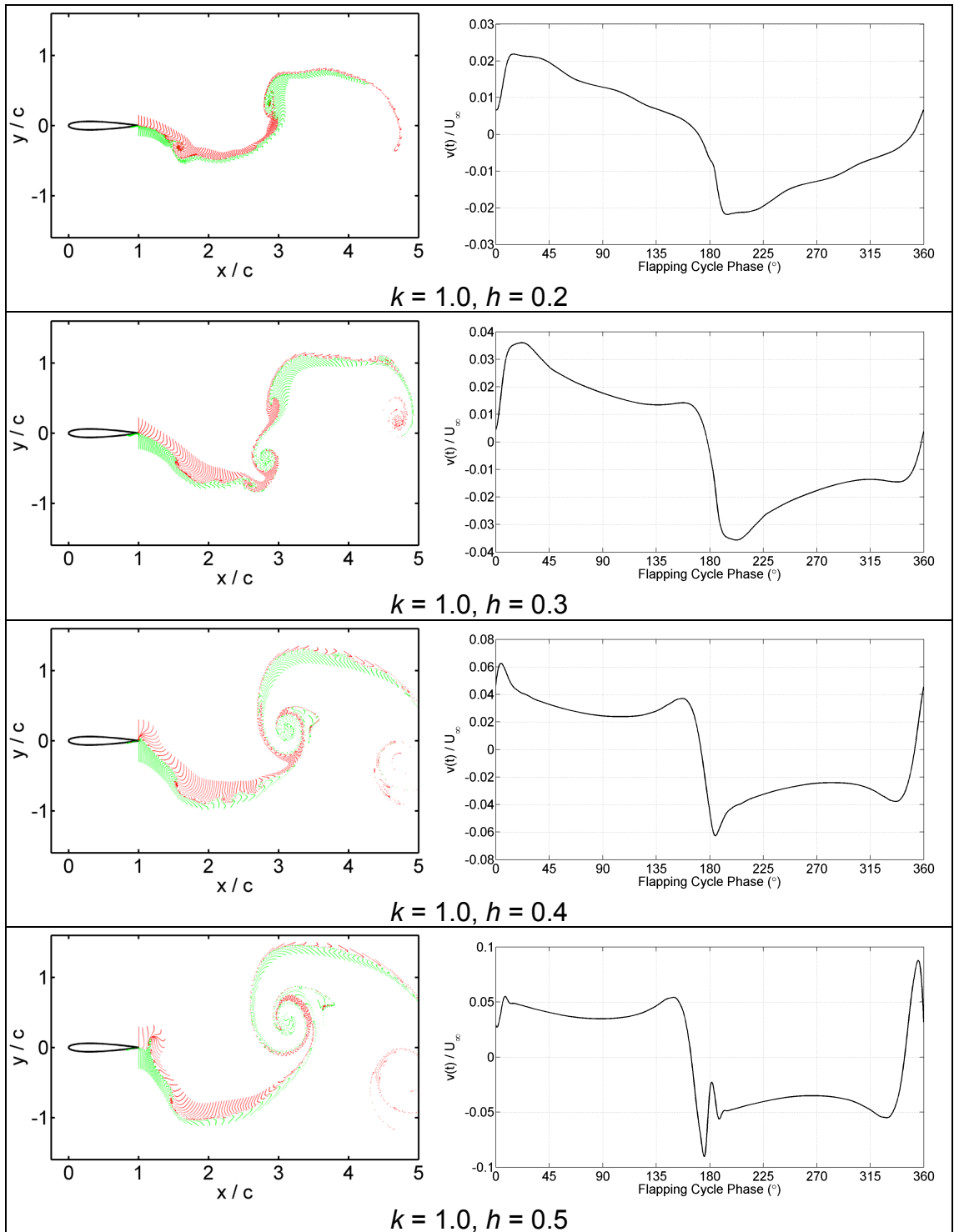


Figure 5.36. NS wake particle traces (left), and vertical velocity time history in the wake (right), showing onset of vortex lock-in with increasing plunge amplitude h , between approximately $h = 0.05$ and $h = 0.2$. Velocity measured at the fixed location in the wake: $x/c = 1.5$, $y/c = 0.0$. $k = 1.0$, $Re = 20,000$.

In the fourth frame ($k = 1.0$, $h = 0.1$), the particle trace appears to show a qualitatively different shedding behaviour. The velocity time history has become periodic at $h = 1.0$, and the superimposed natural shedding frequency has now changed to a harmonic of the flapping frequency.

As the plunge amplitude h is increased further an integer number of vortices is shed per half-cycle, and the number of vortices appears to decrease with increasing h . Figure 5.36 shows that as h is increased, the dominant frequency in the wake is initially the natural shedding frequency, but at a certain critical threshold, the plunging (forcing) frequency becomes dominant.

A similar pattern is observed at higher reduced frequencies. Figure 5.37 and Figure 5.38 show wake particle traces for $k = 5.0$ and $k = 10.0$, respectively. For $k = 5.0$, as for $k = 1.0$, the forcing frequency is below the natural shedding frequency at the Reynolds number considered here ($Re = 20,000$). The first frame of Figure 5.37 ($h = 0.00125$) shows the wake dominated by natural shedding. At $h = 0.0025$ there is some kind of transition process occurring, and at $h = 0.005$ the wake is dominated by shedding at the forcing frequency.

In Figure 5.38 the forcing frequency is now above the natural shedding frequency. For $h = 0.00025$ and $h = 0.0005$ the shedding into the wake is at the natural shedding frequency. At $h = 0.00125$, the dominant shedding mode in the wake has switched to the forcing frequency (this can be seen by counting the number of vortices visible in the wake³).

³ This method of counting vortices is qualitative only. As the plunge amplitude is increased further, the airfoil starts to produce thrust instead of drag and the wake vortices are convected further downstream in the same time, taking some of them out of the view in the frames shown. Thus the more quantitative method of measuring time-histories of the vertical velocity in the wake was applied for $k = 1.0$. However the switchover from natural shedding to forced frequency is quite apparent in the wake particle traces shown.

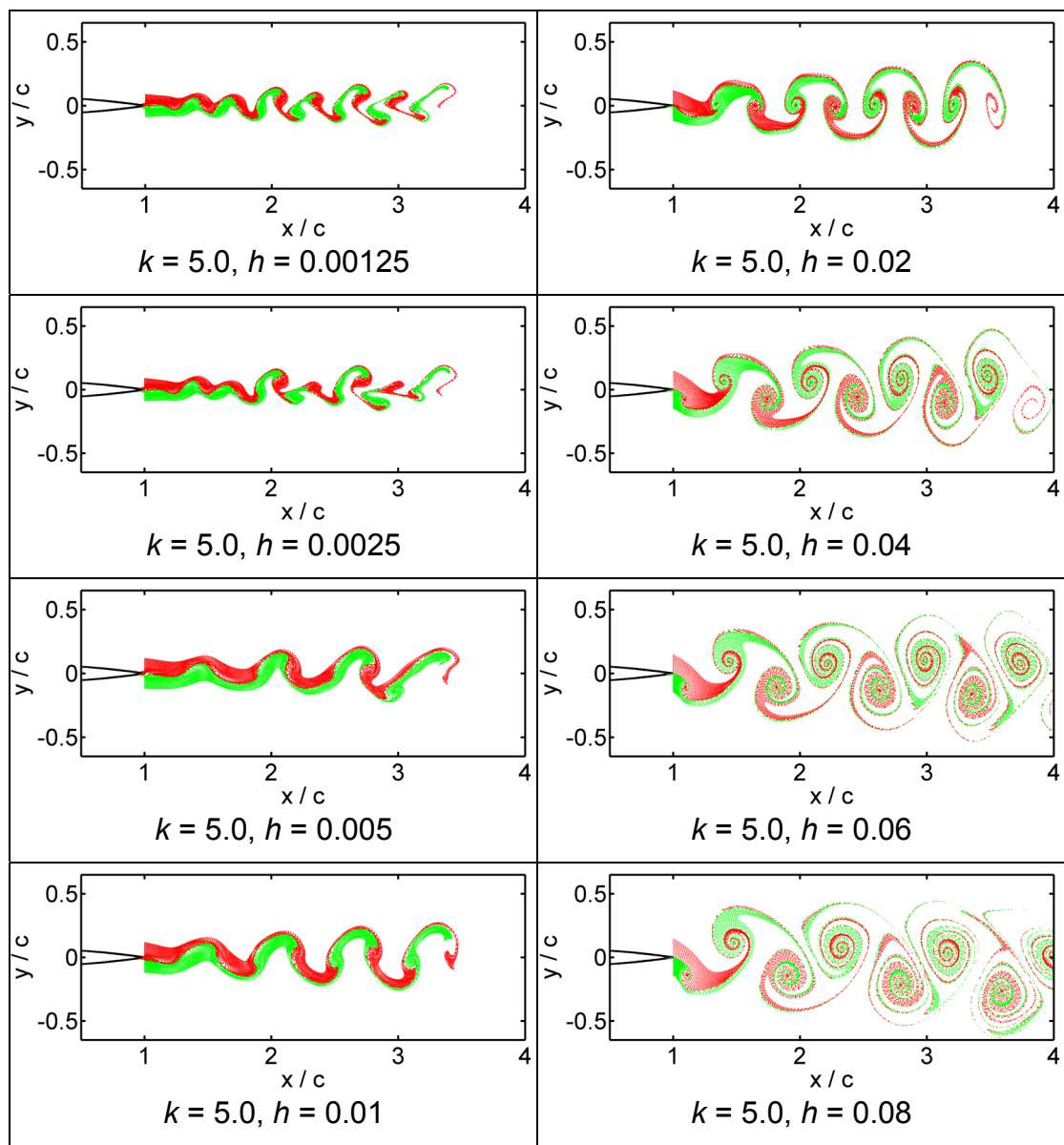


Figure 5.37. NS wake particle traces showing onset of vortex lock-in with increasing plunge amplitude h , between $h = 0.0025$ and $h = 0.005$. $k = 5.0$, $Re = 20,000$.

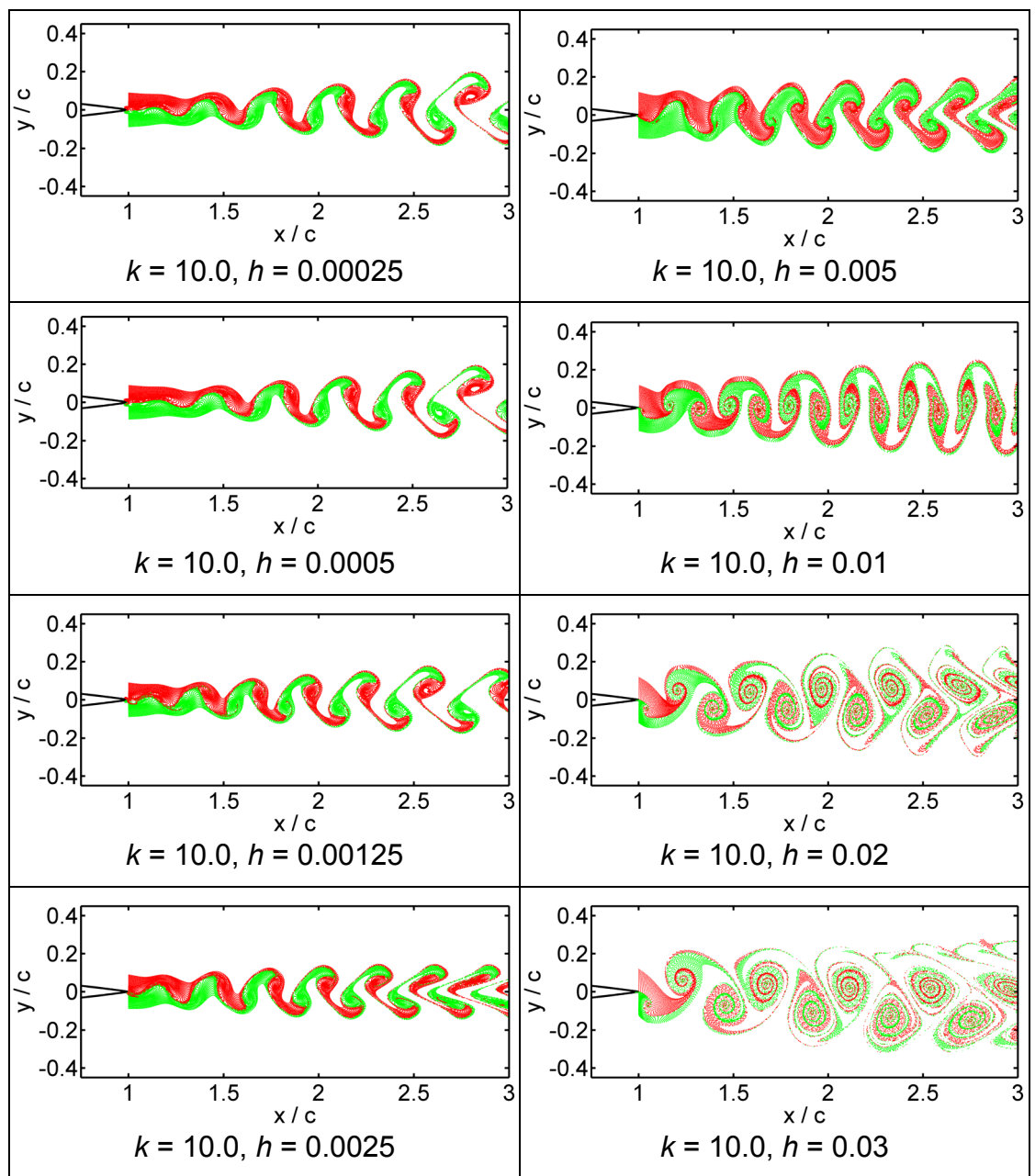


Figure 5.38. NS wake particle traces showing onset of vortex lock-in with increasing plunge amplitude h , between approximately $h = 0.0005$ and $h = 0.00125$. $k = 10.0$, $Re = 20,000$.

An approximate vortex lock-in boundary on the h - k plane, based on the data in Figure 5.36 to Figure 5.38, is plotted in Figure 5.39. This boundary does not follow a contour of constant kh . The plunging frequency is normalised against the natural shedding frequency of approximately $k_{natural} = 9.4$. The boundary divides the h - k plane into regions where either the natural shedding frequency, or the forcing (plunging) frequency dominates the wake.

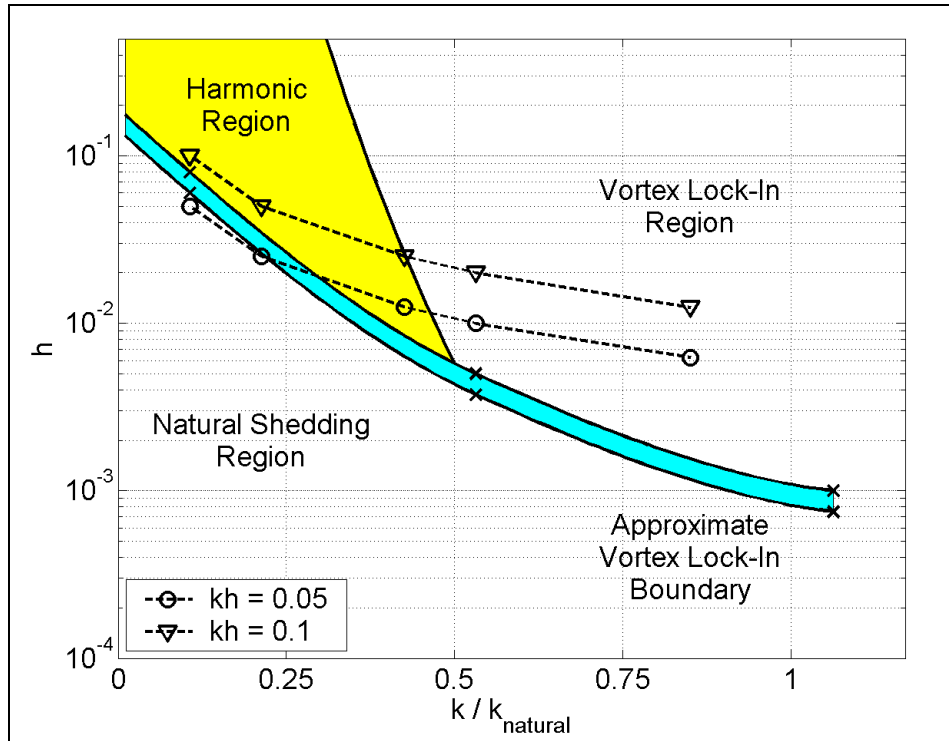


Figure 5.39. Schematic vortex lock-in boundary for a NACA0012 airfoil, at $Re = 20,000$.

By analogy with the receptivity boundary of the circular cylinder case, a ‘harmonic boundary’ is also shown schematically. Inside the harmonic region, the airfoil may display vortex shedding at some higher (integer) harmonic of the forcing frequency. The harmonic boundary must meet the vortex lock-in boundary at $k / k_{natural} = 0.5$, since above this value, any harmonic of the forcing frequency would be above the natural shedding frequency. This is supported by the wake visualisations of Figure 5.36 through to Figure 5.38. For $k = 1.0$, the wake demonstrates a variety of shedding modes as h is increased, whereas for $k = 5.0$ and $k = 10.0$ (both above $k / k_{natural} = 0.5$), the wake changes quite

abruptly from natural shedding to forced shedding with increasing plunge amplitude.

Unlike the circular cylinder case, the vortex lock-in boundary is not likely to be symmetric about the natural shedding frequency. This is due to the sharp trailing edge of the airfoil which fixes the separation point for values of $k > k_{natural}$ and high values of h , and ensures that the shedding takes place at the forcing frequency (i.e. vortex lock-in).

Also shown on Figure 5.39 are two constant- kh contours, at $kh = 0.05$ and $kh = 0.1$. The data points are for k values of 1.0, 2.0, 4.0, 5.0 and 8.0 in each case. If we follow the $kh = 0.05$ contour from low to high frequency, we observe the following behaviour. At $k = 1.0$, the airfoil is in the natural shedding region, and the wake is dominated by the natural shedding frequency as shown for $k = 1.0$, $h = 0.05$ in Figure 5.36. At $k = 2.0$, the airfoil is close to the harmonic region (or perhaps inside, as the boundaries are only drawn approximately), and in the bottom frame of Figure 5.30, the wake for $k = 2.0$, $h = 0.025$ shows a slow variation with more rapid vortex shedding superimposed. At $k = 4.0$ the airfoil is now inside the harmonic region, and the wake for $k = 4.0$, $h = 0.0125$ (middle frame of Figure 5.30) shows two vortices being shed per half-cycle (thus the shedding is taking place at twice the plunging frequency). At $k = 5.0$, the airfoil is now fully inside the vortex lock-in region. This is confirmed by the $k = 5.0$, $h = 0.01$ frame in Figure 5.37, where only the forcing frequency is apparent in the wake particle trace. Finally for $k = 8.0$, the airfoil remains inside the vortex lock-in region, and in the top frame of Figure 5.30 ($k = 8.0$, $h = 0.00625$) we see only the forcing frequency apparent in the wake.

A similar sequence may be followed for the $kh = 0.1$ contour, with wake visualisations presented in Figure 5.32, Figure 5.36 and Figure 5.37. Thus the multiple-vortex-per-half-cycle shedding is shown to be the result of an interaction between the natural shedding frequency of the airfoil at the Reynolds number studied, and the forcing frequency.

It should also be noted that this type of harmonic shedding is not necessarily associated with the change from drag production to thrust production as h is increased for a given k . This may be seen in Figure 5.37, where for values of

$h < 0.02$, the wake shows upstream-tilted vortex pairs characteristic of drag production. At $h = 0.02$ the wake appears ‘neutral’, and values for $h > 0.02$ show the downstream-tilted vortex pairs of thrust production. This may also be seen in Figure 5.38.

5.5 Effect of Turbulence Modelling and Numerical Viscosity in the NS Calculations

The simple algebraic turbulence model used in the calculations, although with a limited range of applicability, was chosen primarily for its simplicity of implementation and widespread use. The intent of the turbulent calculations is to assess the susceptibility of the results to changes in leading and trailing edge separation, rather than to accurately predict the aerodynamic forces due to turbulence. The action of the turbulence model is to increase the effective viscosity in regions of high vorticity.

For $Re = 20,000$, $M_\infty = 0.05$, $k = 4$, $h = 0.0125$, the turbulent viscosity either side of the airfoil trailing edge reaches approximately 10 times the free stream laminar viscosity, and for $k = 4$, $h = 0.075$ it is approximately 60 times higher. This substantially alters the extent of the trailing edge separation region. For the larger airfoil plunging amplitude, this has little effect as the flow over the trailing edge is dominated by the large-scale motion of the airfoil and is effectively forced to flow off the sharp trailing edge, so the laminar and turbulent wakes appear very similar. For the smaller plunge amplitude altering the trailing edge separation has a dominant effect on the appearance of the wake, due to interaction between the plunge frequency and the frequency of vortex shedding off the separated region, which is of the same order of magnitude size as the airfoil motion. Thus the laminar and turbulent cases give rise to very different wakes at small plunge amplitudes and high frequencies, but similar wakes at large amplitudes and lower frequencies. In this way the structure of the wake is dominated by trailing edge effects.

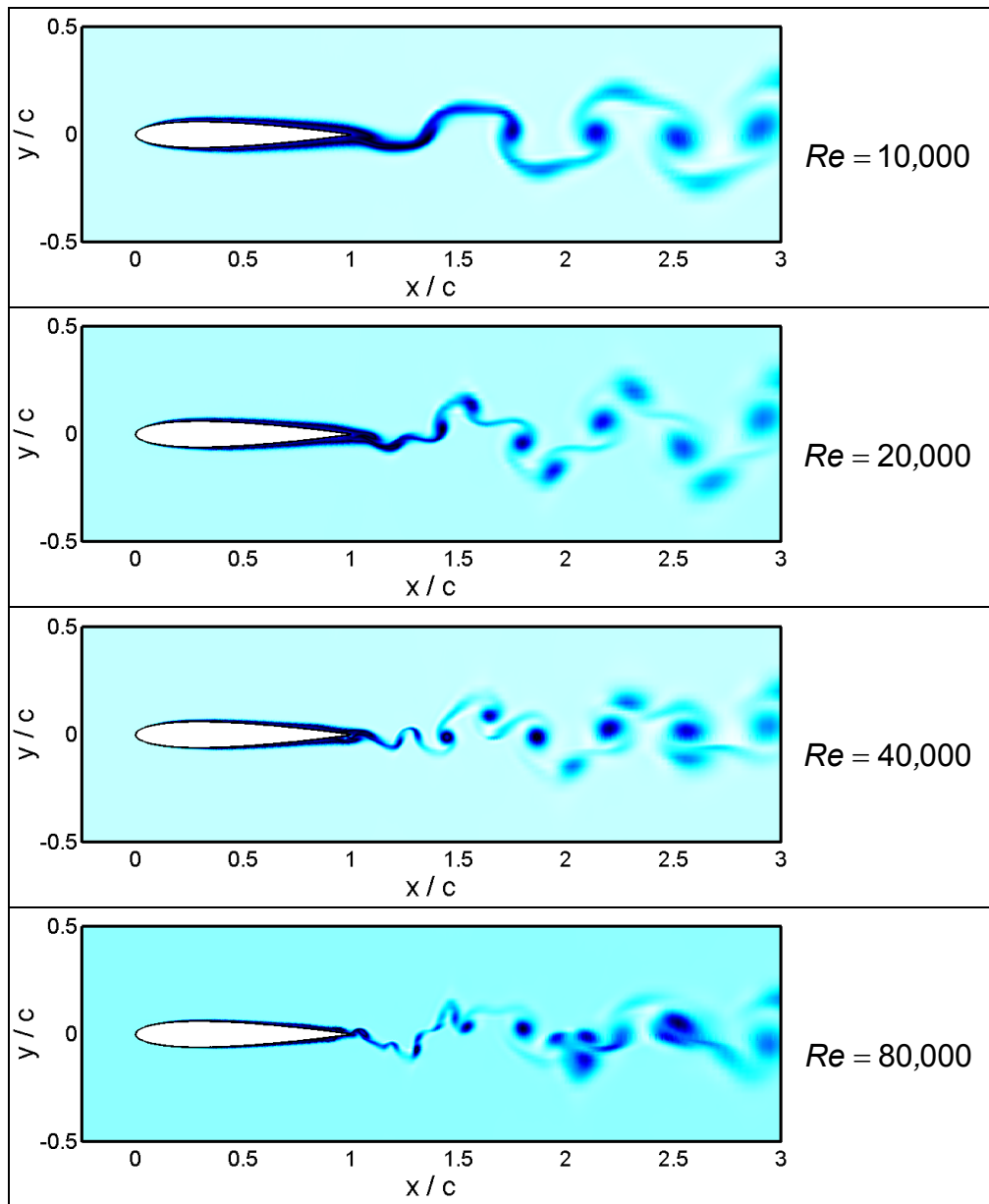


Figure 5.40. Comparison of wake structures via filled contour plots of entropy (p/ρ^γ), $k = 4.0$, $h = 0.0125$, $M_\infty = 0.05$, showing sensitivity of results to free-stream viscosity, inversely proportional to Reynolds number.

The sensitivity of the wake to the additional viscosity introduced by the turbulence model as seen in Figure 5.25 to Figure 5.29 suggests that numerical viscosity is low, at least close to the airfoil where the wake vortices are created. This idea is reinforced by Figure 5.40, which compares results for $k = 4$, $h = 0.0125$ at Reynolds numbers of $Re = 10,000$, $20,000$, $40,000$ and $80,000$ with laminar flow assumed (entropy is plotted here in preference to vorticity as it

captures the filamentary nature of the wake in between vortices more readily than the vorticity for these cases).

Significant variation in the size of the trailing edge separation region, and hence the vortex shedding and wake structure, is observed. Again the apparent sensitivity of the results to this effective change (doubling, halving and quartering) in free-stream viscosity relative to the $Re = 20,000$ results suggests that the wake structures generated by the NS code are governed by physical effects rather than numerical viscosity.

5.6 Summary

The velocity profiles induced by various wake structures were investigated with the VWE (Vortex Wake Evolution) code. Reverse Karman vortex streets were shown to produce a momentum-surfeit (jet) type wake, while Karman vortex streets produced momentum-deficit wakes. A variety of different wake structures was shown to produce neutral (zero net momentum change) conditions.

The wake structure of a plunging NACA0012 airfoil at $Re = 20,000$ was examined across a range of reduced frequencies from $0 < k < 20.0$, using:

- predictions from the Garrick analysis (combined with the VWE code), which assumes a flat plate airfoil, inviscid flow and hence no separation on the airfoil (Kutta condition applied), and small values of the flapping parameter kh ;
- the UPM (Unsteady Panel Method) code, which uses a thick airfoil and allows arbitrary amplitudes of motion, but similarly applies the Kutta condition;
- the NS (Navier-Stokes) flow solver which introduces viscosity and the possibility of flow separation and vortex shedding from locations other than right at the trailing edge; and
- the experimental observations of Lai and Platzer (1999).

Values of $kh < 0.3$ were used, resulting in very small plunging amplitudes at the higher reduced frequencies.

The Garrick + VWE and UPM codes predicted wake structures that were thrust-producing for all flapping parameters. Neither of the two inviscid methods was able to reproduce the multiple-vortex-per-half-cycle shedding seen in the experimental flow visualisations (except when the phase between the vortex strength and the motion was varied arbitrarily in the VWE code). This shedding was determined to be the result of an interaction between bluff-body type natural shedding around the trailing edge, and the motion of the airfoil, at two distinct frequencies. The wake of the airfoil was shown to exhibit ‘vortex lock-in’ as the amplitude of motion was increased.

The vortex lock-in process introduces a flapping frequency dependence into the wake structure of the airfoil. At Reynolds number $Re = 20,000$ the wake is dependent both on reduced frequency k and the flapping parameter kh (equivalent to the Strouhal number) independently, since the natural (bluff-body) shedding has an associated frequency. This frequency dependence is expected to diminish with increases in Reynolds number, as evidenced by the large differences between laminar and turbulent simulations at low flapping amplitudes.

The Kutta condition appears to be violated where natural or harmonic shedding is taking place (i.e. outside the vortex lock-in region of the $h-k$ plane). Inside the vortex lock-in region, the flow does appear to separate off the sharp trailing edge (at the higher flapping amplitudes and kh values), at least on the windward side of the airfoil. In these cases there is little difference between the laminar and turbulent simulations, and the Kutta condition would appear to be valid. This is shown in the following chapter where forces on the airfoil are measured; for a given kh value, at the higher frequencies (inside the vortex lock-in boundary) the NS and UPM codes predict very similar thrust.